https://doi.org/10.59761/RCR5100

Hard carbon — anode material for metal-ion batteries

Elena N. Abramova,[a] Zoya V. Bobyleva,[b] Oleg A. Drozhzhin,[b] Artem M. Abakumov,[a] Evgeny V. Antipov[a,b]

[a] *Skolkovo Institute of Science and Technology, Bolshoy Boulevard 30, stroenie 1, 121205 Moscow, Russian Federation*
[b] *Faculty of Chemistry, Lomonosov Moscow State University, Leninskie Gory 1, stroenie 3, 119991 Moscow, Russian Federation*

The development of large-scale energy storage systems based on matured technology of lithium-ion batteries (LIBs) is hindered by the high cost of Li. Thus, analogous technologies involving other alkali metals (sodium (SIBs) and potassium (PIBs)) are being developed. Among various materials for negative electrodes (anodes) for such batteries, carbon materials are the most promising; in particular, hard carbon is of special interest. The review is devoted to the state-of-the-art research on the structure, composition and properties of this type of material, as well as to the analysis of methods for its preparation and study. The description of the microstructure of hard carbon is an extremely ambiguous and unresolved issue, therefore the review pays special attention to various microstructural models. It also systematizes synthesis methods and analyzes the results of studies of the physicochemical properties of hard carbon. It reveals fundamental trends and correlations between production technologies, material characteristics and electrochemical performance of hard carbon materials. A large number of results of electrochemical studies are analyzed, the ideas about the mechanisms of electrochemical interactions of Na^+ and K^+ cations with hard carbon are systematized, and the contradictions existing in the various models of the mechanisms of such interactions are shown.
The bibliography includes 247 references.
Keywords: metal-ion batteries, carbon-based anode materials, hard carbon, materials research techniques, electrochemical performance.

Contents

1. Introduction

The continuous growth of energy consumption has led to the development of energy storage technologies. The most effective of them are based on the use of batteries as electrochemical power sources. Widely used lead-acid batteries suffer from a number of disadvantages, the most important of which are low specific capacity (25–40 W h kg^{-1}),[1] short lifetime, high toxicity of lead.

Lithium-ion (Li-ion) batteries have none of these drawbacks, therefore they now dominate the market for portable electronics and electric transport.[2] However, the use of Li-ion batteries for many large-scale applications (stationary energy storage, power plant buffer systems, electric passenger transport, *etc*.) is hampered by the high cost of lithium and by the fact that its natural sources are localized at a few places in the world. Replacing lithium with its alkali metal analogues (sodium and potassium) appears to be a promising alternative due to the abundance of Na and K in the Earth's crust (2.5 and 1.7 wt.% respectively)[3] and their low cost compared to lithium. In addition, lithium forms alloys with aluminum during electrochemical charging, forcing battery manufacturers to use more expensive and heavier copper foil as the current collector for the negative electrode (anode). Sodium and potassium are

Received 18 August 2023

free of this shortcoming, so aluminum foil can be used both for positive electrodes (cathodes) and for anodes, which is an additional factor in reducing the cost of sodium and potassium ion batteries (SIBs and PIBs) due to the lower cost of aluminum. It is also worth noting the fundamental similarity of LIB, NIB and PIB technologies, which makes it possible to apply the technological solutions developed for LIB to SIB and PIB, including those for the production of electrodes, cells, batteries, monitoring and control systems.

In addition, the electrode potentials of the Na/Na^+ and K/K^+ redox pairs in the propylene carbonate-based electrolyte are close to the electrode potential of the Li/Li^+ pair (higher by 0.23 V and lower by 0.09 V respectively).[4] This allows for high operating voltage and energy density of SIBs and PIBs and makes their characteristics potentially comparable to those of LIBs. Despite the fact that sodium and potassium ions have larger weights and sizes relatively to lithium ions (the ionic radii of Na^+ and K^+ are 1.02 and 1.38 Å, respectively, the ionic radius of Li is 0.76 Å), the sizes of solvated sodium and potassium ions in propylene carbonate are 4.6 and 3.6 Å, respectively, which is smaller than the Stokes radius of lithium ions (4.8 Å).[5] Therefore, electrolytes for Na-ion and K-ion electrochemical systems may have higher ionic conductivity, which will reduce the overall resistance of SIB and PIB cells.[5]

Cathode materials for these electrochemical systems include polyanionic compounds (*e.g.*, phosphates, fluoride phosphates, *etc.*), oxide materials and Prussian blue analogues. The specific capacity of SIB and PIB cathode materials is lower than similar metrics of LIB materials, which is mainly due to higher values of ionic radii and atomic weights of potassium and sodium.

Among the various anode materials for metal-ion batteries, carbonaseous materials have attracted the most interest[6–10] due to their low cost, high electronic conductivity and ability for reversible electrochemical interaction with sodium and potassium ions. However, graphite, which is widely used as an anode material in LIBs, has an extremely low specific capacity (~35 mA h g^{-1}) in SIBs and a significant volume change of the material (up to 61%) in PIBs, which makes it technologically unpromising in both cases.[11,12] In this context, the attention of the researchers and developers of SIBs and PIBs is drawn to other carbon materials, primarily hard carbon. However, it should be noted that the main research is focused on the use of hard carbon as an anode material in sodium-ion electrochemical systems. The reasons for this seem to be the high performance characteristics of hard carbon in SIBs (specific capacity, cycling stability, Coulombic efficiency), as well as a higher maturity of the technology itself compared to PIBs, which prospects are not rather clear.

The first review devoted to the use of hard carbon as an anode material for SIB appeared in 2015.[3] In this paper, the authors used results from the study of their own samples by gas adsorption-desorption, X-ray diffraction and Raman spectroscopy to describe the properties of the material. However, there was no comparison of these results with those of other authors. The main focus of this paper was the electrochemical properties of hard carbon in sodium-ion electrochemical systems.

Mittal *et al*.[13] gave general characteristics of hard carbon and noted that the morphology of the material depends on the synthesis conditions. The main issue of this paper is the mechanism of electrochemical interaction of hard carbon with sodium cations and a review of methods for studying the material. Another review[14] also highlights the electrochemical properties of hard carbon in sodium-ion systems. It classifies models of the interaction of the material with Na^+, considers practical issues of the synthesis of hard carbon and the preparation of sodium-ion batteries with improved electrochemical properties.

A comprehensive analysis of the microstructure of hard carbon is given in another review paper.[15] It should be noted that reviews devoted to hard carbon in SIBs require additions summarizing the results of characterization of its composition and structure using modern research methods. The application of this material to other electrochemical systems, such as PIBs and LIBs, is also relevant for generalization and analysis.

The subject of the present review is therefore hard carbon as a material for negative electrodes of metal-ion batteries. It has several objectives: 1) to reflect the state-of-the-art understanding of the microstructure of hard carbon and the mechanisms of its interaction with alkali metal cations; 2) to systematize the methods used in materials research and the information obtained from them; 3) to find out the correlations between the methods of synthesis of hard carbon, its microstructure and electrochemical properties; 4) to analyze the results of the application of this material in three electrochemical systems — LIBs, SIBs and PIBs.

2. The definition of hard carbon and 3 models of its microstructures

Among all the variety of anode materials, a special role in the development of SIBs and PIBs is played by non-graphitizable carbon (or non-graphitic carbon, also termed as ‘hard carbon’).

The term ‘hard carbon’ refers to carbon materials that are not graphitized by heat treatment at high temperature, up to 3000 °C, in an inert environment. Samples of hard carbon have a

E.N.Abramova. PhD, Research Scientist at Skoltech.
E-mail: El.Abramova@skoltech.ru.
Current research interests: metal-ion batteries, anode materials, new functional materials.
Z.V.Bobyleva. PhD, Research Scientist at the Department of Electrochemistry of the Faculty of Chemistry of MSU.
E-mail: zoyamostovik@gmail.com.
Current research interests: carbon-based anode materials, electrolytes for metal-ion batteries.
O.A.Drozhzhin. PhD, Senior Researcher at the Department of Electrochemistry of the Faculty of Chemistry of MSU.
E-mail: drozhzhin@icr.chem.msu.ru.
Current research interests: metal-ion batteries, cathode materials, anode materials, electrolytes for metal-ion batteries.
A.M.Abakumov. PhD, Director of the Skoltech Center for Energy Science and Technology (CEST), Professor at Skoltech.
E-mail: a.abakumov@skoltech.ru.
Current research interests: crystal chemistry of inorganic compounds, solid state chemistry, metal-ion batteries, crystallography, chemistry of complex oxides, transmission electron microscopy, X-ray diffraction, neutron diffraction, modulated structures, magnetic structures.
E.V.Antipov. PhD, DSc, Professor, Corresponding Member, Head of the Department of Electrochemistry at the Faculty of Chemistry of MSU. E-mail: antipov@icr.chem.msu.ru.
Current research interests: inorganic materials for electrochemical power sources: metal-ion batteries and power cells, superconductive inorganic materials.

Translation: N.M.Vinogradova.

disordered microstructure which differs from that of graphitizable carbon (termed as 'soft carbon').[16,17] If graphitizable carbon gradually forms the graphite structure during high-temperature pyrolysis, the 'final' form of non-graphitizable carbon is glassy carbon.[18] This is why many studies of the macro- and microstructure of hard carbon are closely intertwined with studies of glassy carbon.[19,20]

The first models of the structure of hard carbon were proposed in the 1950s. Among them, it is worth mentioning the packet and fringe model (other names include fringed micellar, crystallite) (Fig. 1*a*), proposed by V.I.Kasatochkin (see[21] and references therein). Another model, the 'house of cards' one, was proposed by R.Franklin[22,23] in 1951 (Fig. 1*b*). According to these models, hard carbon is a set of randomly arranged crystallites (domains) consisting of several graphitic atomic planes (4–6 layers) with a lateral size of about 40 Å. The domains are in turn connected by a 'fringe' of linear carbon chains.

It was later suggested (Jenkins' model, 1972, Fig. 1*c*),[24] that hard carbon consists of intertwined graphitic ribbons — randomly oriented and interconnected twisted microfibrils with a higher concentration of voids and hence lower material density than graphite (~1.5 *vs* 2.3 g cm^{-3}).

A new concept of the microstructure of hard carbon is based on the model of P.Harris (1997) developed as a result of the active study of fullerene-like structures.[25–27] According to this model, hard carbon consists of fragments of bent graphene-like layers containing five-, six- and seven-membered rings (Fig. 1*d*).

At present, machine learning methods have greatly simplified the modelling of the microstructure of amorphous hard carbon. Recent studies[28,29] have shown that the density of hard carbon is inversely proportional to the diameter of the micropores. It was found[28] that five- and seven-membered rings are inherent in the microstructure of amorphous carbon, but that five-membered motifs are more common than seven-membered or other, rarer, types of defects in the graphene-like sheet, for example Stone-Wales defects (which arise due to rotations of C–C bonds through an angle of ~90° in the hexagonal structure, bringing two pentagonal and two heptagonal rings into the structure).

Hard carbon has defects, mainly in the form of dangling bonds at the edges of graphite-like domains and vacancies in graphene-like layers. In addition, these materials often contain heteroatoms such as O, N, S (the latter found in the case of nitrogen- or sulfur-containing precursors used for synthesis). The ratio of carbon atoms with different types of hybridization, the presence of heteroatoms, as well as material parameters such as porosity, defectiveness, *etc*. are determined by the choice of precursor and synthesis conditions. The microstructure of hard carbon, including the mutual arrangement of atoms and groups of atoms, layers of carbon atoms, hybridization of C atoms, as well as micropores of the material resulting from the peculiarities of the mutual arrangement of layers of C atoms, defects in the material, remains a relevant and fundamentally important issue for the understanding of the mechanism of intercalation/deintercalation of alkali metal ions and the optimization of the microstructure of the material for its practical application.

3. Synthesis of hard carbon

Hard carbon materials are obtained by high temperature annealing (pyrolysis) of organic raw materials in an inert atmosphere. The synthetic route can be divided into several stages: pretreatment of the precursor, high-temperature annealing of the pretreated product or pure precursor, and sometimes post-processing of the annealed product.[30]

The precursors most commonly used to produce hard carbon can be broadly categorized into carbohydrates, including cellulose,[31–36] and synthetic polymers such as PAN (polyacrylonitrile), PET (polyethylene terephthalate), PFA (perfluoroalkoxide polymers), phenolic resins and pitches,[37,38] lignin.[39–45] Since hard carbon is a very promising material for large-scale production, a number of environmentally friendly technologies are being developed to produce it from a variety of low-cost materials, including biomass.[46–68] For example, Lakienko *et al*.[69] have recently proposed a technology for the production of hard carbon from Sosnowskyi hogweed, an invasive and widespread plant. The key step in the proposed synthesis is acid washing prior to carbonization, which helps to improve the Coulombic efficiency of the first charge-discharge cycle up to 87% (initial Coulombic efficiency, ICE).

The choice of precursor is determined by its availability in the region, the cost and the yield of hard carbon. Irisarri *et al*.[70] noted a high yield (50%) of product derived from phenol formaldehyde resin compared to that from lignin and microcrystalline cellulose. A high product yield (40–67%) is also typical for PAN-derived hard carbon.[71] Górka *et al*.[72] considered biomass as a cheap precursor for the hard carbon, but reported low yields of hard carbon derived from biomass and various sugars (up to 10%) except for lignin (up to 50%). Abramova *et al*.[73] reported a higher yield of hard carbon (10–28%) when polytetrafluoroethylene (PTFE) was added to sucrose.

The production of hard carbon is quite similar to the technological process of producing activated carbon, since the key step of the synthesis is also high-temperature annealing.[74] The main difference is that the production of hard carbon anode materials does not require the activation step, as the creation of

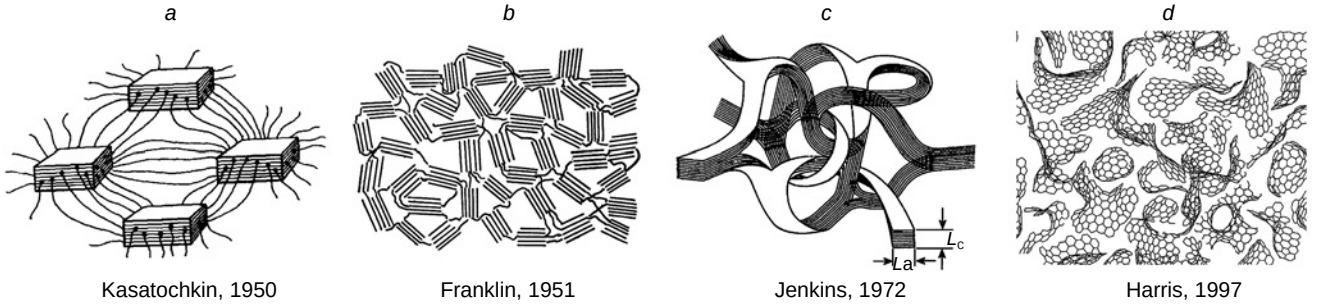

Figure 1. Hard carbon microstructure models: (*a*) packet and fringe Kasatochkin's model,[21] (*b*) 'house of cards' Franklin's model,[22,23] (*c*) Jenkins' model[24] and (*d*) Harris' model.[25]

mesoporosity contributes to the deterioration of the electrochemical properties.

The first step of the synthesis is usually a preliminary heat treatment of the precursor in air at temperatures above 100 °C. The main objectives of the pretreatment are dehydration of the feedstock and formation of the desired morphology of the precursor. Thermal pretreatment of sugars is called caramelization. It is a well known process in the food industry. Pretreatment is also carried out under hydrothermal, solvothermal and microwave hydrothermal conditions.[75–78] Varying the conditions of this process makes it possible to obtain micro- or nanoparticles of microspherical shape. Both caramelization and hydro- and solvothermal carbonization are complex processes. During caramelization, the crystalline structure of the sugars is destroyed to give amorphous glasses with different C:H:O ratios.[79] In hydro- and solvothermal carbonization, sugars are hydrolyzed to form monosaccharides, which subsequently undergo dehydration and condensation and produce both liquid and solid carbon-rich products.[79] The temperature of the process is chosen according to the composition of the precursors.[56,65,80] Pretreatment is not a mandatory step in the synthesis of hard carbon, but pre-dehydration followed by high-temperature carbonization results in a material with a lower specific surface area, which usually improves the — ICE.[35] Bobyleva *et al.*[81] showed that the conditions of thermal pretreatment of glucose in a narrow temperature range (200±40 °C) have a decisive influence on the morphology and specific surface area of hard carbon. It has been found that reducing the specific surface area, the degree of defectiveness and the oxygen content on the surface can improve the ICE of hard carbon up to 89% in sodium-ion half-cells.

Pretreatment is also carried out to remove impurities such as potassium, calcium, magnesium and silicon, which are present in biomass.[72] Washing with water or solutions of acids and alkalis removes impurities and has a positive effect on the electrochemical properties of the biomass-derived hard carbons.[64,82–84]

The key step in the synthesis of hard carbon is carbonization — high temperature annealing at temperatures between 900 and 2600 °C in an inert atmosphere. During this stage, heteroatoms and remaining functional groups are removed from the precursor or a pretreated carbonaceous product.[85] As the temperature increases, the ratio of carbon to oxygen and other heteroatoms increases significantly. For the glucose-derived materials subjected to hydrothermal pretreatment, the molar ratio of carbon to oxygen, as determined by X-ray photoelectron spectroscopy, changes from 15.9 at 1000 °C to 74.9 at 1900 °C.[86]

Carbonization temperatures up to 1000 °C do not allow removing of a significant portion of heteroatoms, which affects the electrochemical performance of the material, as sodium and potassium ions are able to interact with heteroatomic functional groups.[71] Such interaction is mostly irreversible, so higher carbonization temperatures are used for the synthesis of hard carbon, as this helps to improve the electrochemical properties.

A number of studies confirmed the dependence between the electrochemical properties, capacity and Coulombic efficiency of the anode material and the carbonization temperature for various precursors (see, *e.g.*, Ref. 85). This dependence is not direct — for example, the maximum capacity for hard carbon in SIBs can be reached as annealing temperatures varies in the range of 1300–1500 °C. With further increase in temperature, the capacity begins to decrease (Fig. 2). The nature of this process and possible reasons for the decrease in capacity are discussed below.

It should be noted that although the annealing temperature of 1300–1500 °C makes it possible to obtain materials with good electrochemical performance, attempts are being made to reduce it to 1000–1100 °C in order to reduce the energy costs of

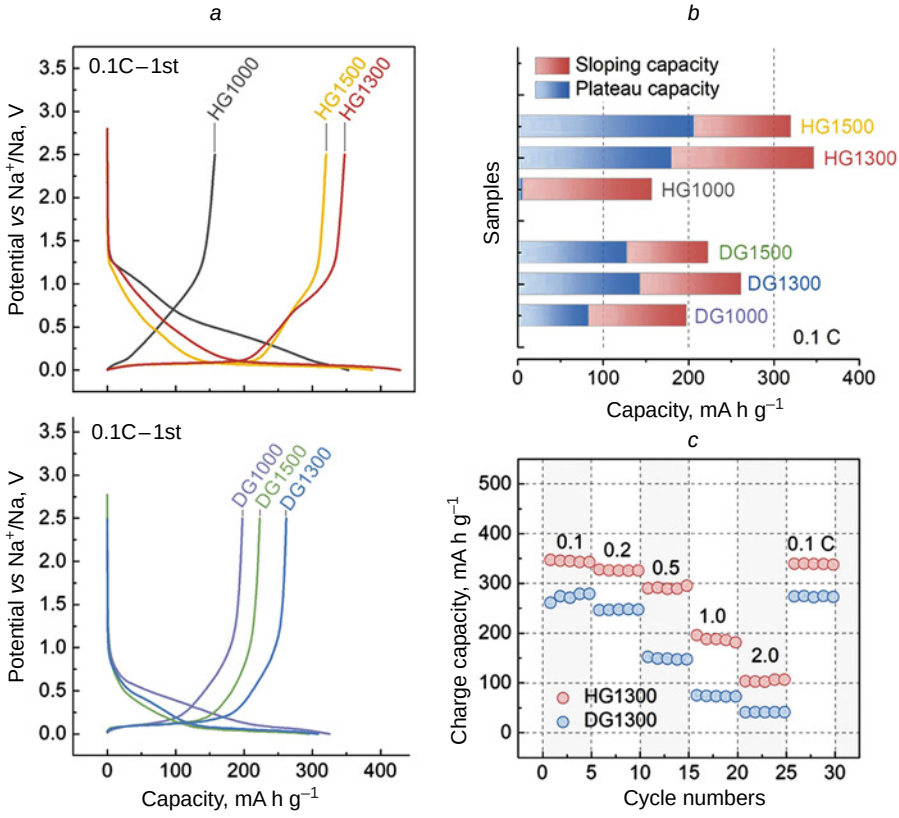

Figure 2. (*a*) Galvanostatic charge/discharge curves of hard carbons obtained *via* hydrothermal carbonization followed by annealing (HG samples) or *via* direct annealing (DG samples) of glucose at different annealing temperatures (from 1000 to 1500 °C) for the same samples: (*b*) difference in slope and plateau capacities; (*c*) cyclic performance at different current densities.[78]

material production and the corresponding technological challenges.[87] Problems associated with the presence of heteroatoms and the high specific surface area of such materials are solved by more complex pretreatment of the precursor, as well as the use of dehydrating agents that help to remove water therefrom.

The post-processing of hard carbon includes grinding in a ball mill, removal of mechanical impurities from the material and additional drying to remove adsorbed water from the carbon surface prior to preparation of the electrode slurry.

There are other less common methods of synthesis of hard carbon, such as

1) plasma-chemical synthesis, which involves deposition of nano-sized carbon on a carrier from a gaseous medium containing hydrocarbons (*e.g.* xylene[60]) and plasma generated by a vacuum-arc discharge;

2) laser ablation of carbon fibres;[88]

3) template synthesis, widely used to prepare carbonaceous materials with micropores. Zeolites,[89,90] silica,[91] magnesia[92] and zinc oxide[93–95] can be utilized as the template. After carbonizing a mixture of the template and precursor, the former is washed out using alkali or acid solutions. To reduce the specific surface area, the carbonaceous material obtained after washing is subjected to repeated carbonization.[92]

As a rule, the presence of heteroatoms, impurities degrade the electrochemical performance of hard carbon due to irreversible interaction with sodium/potassium cations. However, there is an area of research aimed to make this interaction reversible, which will allow to improve the electrochemical capacity of doped hard carbon materials. The main dopants are nitrogen,[96–98] sulfur,[99,100] phosphorus[101] and boron.[102,103] To prepare doped hard carbons, special precursors are used which already contain the necessary heteroatoms. For example, to obtain nitrogen-doped carbon materials, polymer precursors are used such as PAN,[71] polyaniline (PANI)[104] and polypyrrol (PP).[105,106] The doping process can also be carried out through carbonization of the precursor in a mixture with a source of heteroatoms, or by annealing in an inert atmosphere with the addition of gases containing the required heteroatoms.[107] Also of interest is the co-doping of hard carbon material with multiple heteroatoms to create a larger number of probable interaction sites and boost the discharge capacity.[108–111]

4. Methods for studying the composition and structure of hard carbon

A number of modern analytical methods are used to study hard carbon. The main methods for studying the chemical composition of hard carbon include CHNS/O elemental analysis, energy-dispersive X-ray spectroscopy (EDS) and X-ray photoelectron spectroscopy (XPS), particles morphology and open pores are studied using scanning electron microscopy (SEM) and gas adsorption/desorption, respectively. The microstructure of the material under consideration is studied by means of transmission electron microscopy (TEM), X-ray diffraction (XRD), Raman spectroscopy, pair distribution function (or pair distance distribution function (PDF)) based on the analysis of X-ray total scattering, synchrotron and neutron scattering data, small-angle X-ray scattering (SAXS), atomic force microscopy (AFM), scanning tunnelling microscopy (STM), electron paramagnetic resonance (EPR) and others techniques.

When studying hard carbon by various methods, the data obtained are usually compared with those of graphite (Fig. 3). Figure 3 shows the results of studies on these materials using different techniques.

4.1. Chemical composition

Elemental analysis is widely used to study the chemical composition of hard carbon. It helps to determine the chemical composition of both the final material and the products of the processing of precursors at different stages of the hard carbon production. Titirici *et al.*[113] showed that the precursors obtained *via* the hydrothermal treatment of various raw materials (sugars, dehydrated hydrocarbon derivatives, *etc.*) contain the elements C, O, H. Examination of hard carbon after the high-temperature carbonization shows that it consists predominantly of carbon, irrespective of the starting materials, and that as the annealing temperature increases, the carbon atom ratio increases while the ratio of other atoms decreases.[58,114] As the annealing temperature is further increased, the ratio of O atoms becomes comparable to the measurement error.

XPS is another method of studying the chemical composition, which provides data on the chemical composition of the surface of hard carbon samples.[115–121] Figure 4 shows a typical XPS spectrum of hard carbon.

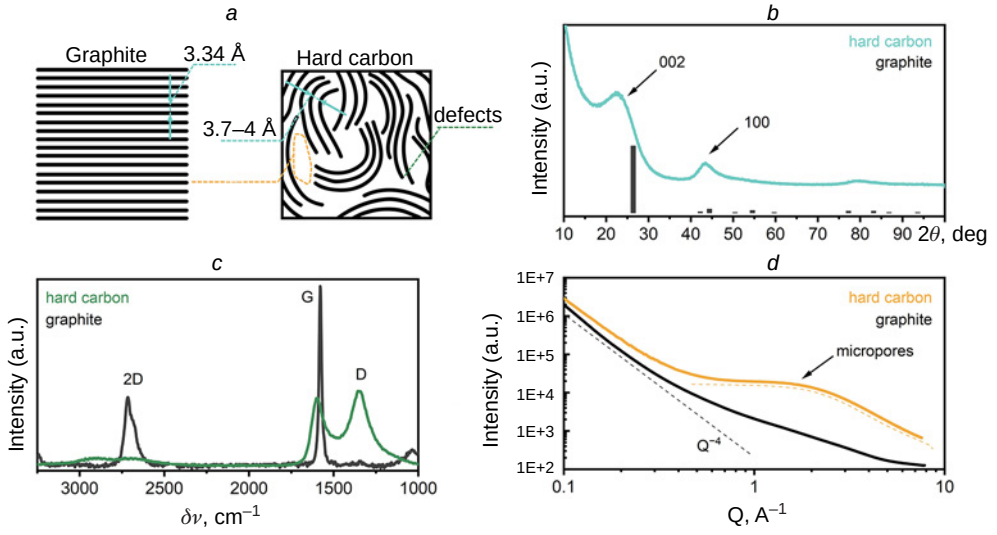

Figure 3. (*a*) Schemes of graphite and hard carbon structures (graphene-like sheets are indicated by black bars); (*b*) X-ray diffraction pattern of hard carbon and position of X-ray reflections of graphite; (*c*) Raman spectra; (*d*) small-angle X-ray scattering spectra.[15,85,112]

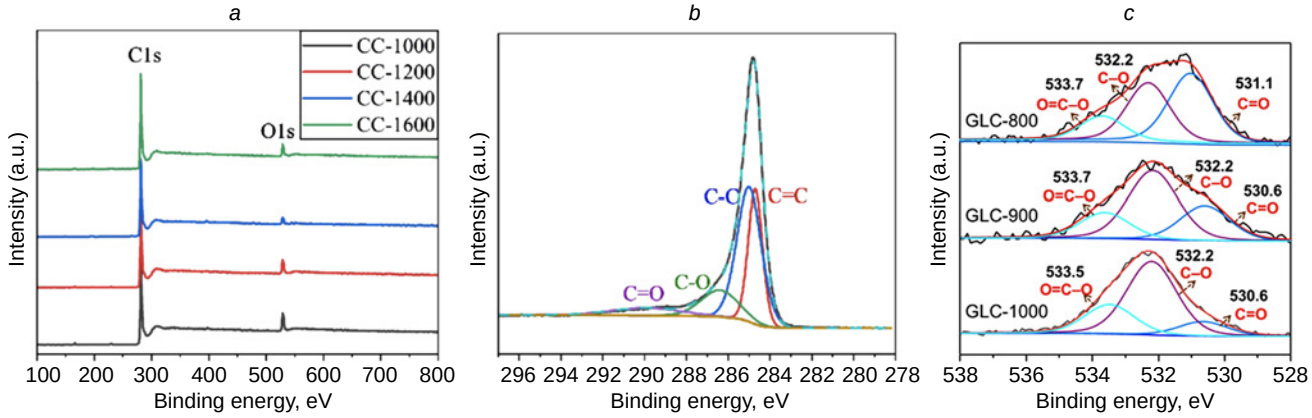

Figure 4. XPS spectra of hard carbon samples obtained from corncobs at different carbonization temperatures: (*a*) wide spectrum,[115] (*b*) fitted C1s XPS spectra of a sample carbonized at 1000 °C;[115] (*c*) fitted O1s spectra of *Ganoderma lucidum* residue-derived samples carbonized at 800, 900 and 1000 °C.[117]

The XPS spectra indicate that the surface of hard carbon contains carbon as the main component, corresponding to the C1s line. In various studies, this peak is characterized by binding energies in the range of 280 to 292 eV.

Moreover, oxygen is often found on the surface of hard carbon. Oxygen-containing functional groups are detected in the energy range of the C1s peak as well as at binding energies of around 532 eV, where the O1s spectral line is identified. Among the oxygen-containing groups, (C–O), (C=O), (O–C=O), (COOH), (C–OH) and the H_2O molecule have been identified in various studies.[11,31,32,55,57,64,65,68,71,116–121]

In addition to carbon and oxygen, nitrogen-containing groups (C–N), (C=N), (N–C=O) have also been detected on the surface of hard carbon by the XPS technique.[55,64,116,117,120] In addition to the above atoms, small amounts of P and S were detected in the *Ganoderma lucidum* residue-derived material.[117]

The studies on the composition of hard carbon samples carbonized at different temperatures show that the content of heteroatoms decreases with increasing carbonization temperature, in particular the content of oxygen groups (C=O) and (C–O). At the same time, the (C=O) peak decreases faster than that of the (C–O) group (Fig. 4*c*).[117] This may influence the mechanism of energy storage in the material (as noted by the authors of paper,[117] a reversible reaction — C=O+Na++e- ↔ –C–O–Na is possible).

4.2. Morphology of materials

SEM is the main method used to study the morphology of hard carbon. Comparison of SEM images of samples obtained from different precursors by different processing techniques[16,31,32,41,52,55–58,64,65,68,80,116,117,121–129] shows a great diversity in the morphology of the materials. The particles of samples derived from carbohydrates by caramelizing the precursor in air at 180 °C before carbonization (Fig. 5*a*),[81] have an asymmetric shape that depends on the milling conditions of the sample.[81,130,131] Hard carbon samples obtained from glucose or sucrose by hydrothermal pretreatment at 180 °C are characterized by spherical particle shapes (Fig. 5*b*).[34,73,131] It is worth noting that it is extremely difficult to favour one or the other type of morphology, as both types of materials can exhibit quite attractive electrochemical performance.

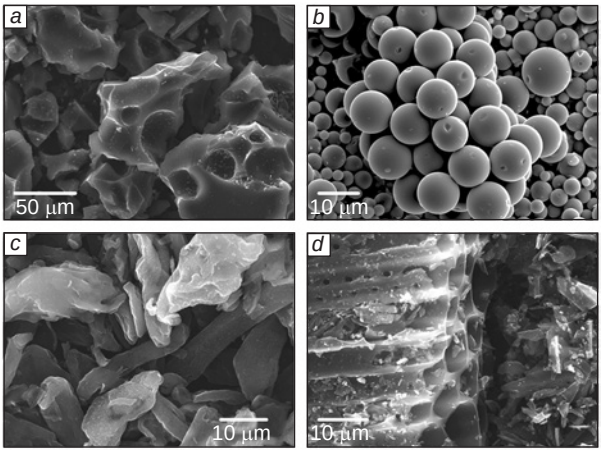

Figure 5. SEM microphotographs of hard carbon samples derived from: (*a*) glucose *via* caramelization (the image was taken from authors archive to Ref. 81); (*b*) glucose *via* hydrothermal carbonization (the image was taken from authors archive to Ref. 73); (*c*) cellulose (the image was taken from authors archive to Ref. 131); (*d*) Sosnowskyi hogweed (the image was taken from authors archive to Ref. 69).

Analysis of the morphology of hard carbon samples derived from different biomasses indicates that it inherits the morphology of the starting materials (Fig. 5*c*,*d*).[69,131]

4.3. Microstructure of hard carbon

High resolution TEM and electron diffraction, Raman spectroscopy, XRD and PDF methods are used to study the microstructure of hard carbon. The key challenges solved by these methods are to determine the influence of synthesis conditions on the microstructure of hard carbon (due to the special scientific and practical interest, the study of defects is considered in a separate Section).

For example, Zhang *et al.*[71] showed that PAN-derived hard carbon has a highly disordered microstructure at a carbonization temperature below 1000 °C. As the carbonization temperature is increased up to 2000 °C, the formation of randomly oriented domains consisting of bent sheets of carbon atoms is observed. Further increase in the carbonization temperature result in a significant rise in the domain length. Damodar *et al.*[126] found that in hard carbon obtained from sepals of Palmyra palm fruit

calyx, the appearance of domains of several graphene-like layers is observed already at the carbonization temperature above 700 °C and there is a tendency to increase the number of such domains with increasing carbonization temperature. Similar changes, from virtually amorphous microstructure to the formation of nano-sized graphite-like domains, are also observed in the natural cotton biomass-derived hard carbon[125] with increasing carbonization temperature from 1300 to 1600 °C. Simone *et al*.[132] also observed an increase in ordering of the samples of cellulose-derived hard carbon with increasing carbonization temperature. TEM clearly shows an increase in the degree of graphitization of the material with increasing carbonization temperature (Fig. 6).[57,59,80,117,127,132,133] This trend is also confirmed by electron diffraction: a number of publications[51–53,65,74,113,116,119,123] report a decrease in the width of the diffraction rings with increasing carbonization temperature. It indicates an increase in structural ordering. At the same time, the temperature of graphite-like domains genesis varies for different precursors and depends on their pretreatment.

It is worth noting that during carbonization of hard carbon derived from various precursors (*e.g*. coffee waste,[128] resorcinol-formaldehyde resin[134]) at temperatures above 2000 °C, a tendency towards further ordering of the microstructure is observed. The increase in temperature from 2000 to 3000 °C causes parallel sheets of carbon atoms to first bend and then straighten during carbonization up to 2500 °C, but graphite formation does not occur.

In addition to visualizing the material microstructure, a number of studies[59,64,65,68,124,125] have used high-resolution TEM to determine the distance between the layers of carbon atoms (d) in graphite-like domains, which typically varies from 0.37 (Ref. 59) to 0.44 nm (Ref. 64) depending on the carbonization temperature of the samples. It should be noted that these values are always larger than d_{002} of graphite (0.335 nm).

Similar results are obtained with PXRD. X-Ray diffraction patterns of hard carbon show two strongly broadened reflections at $2\theta \sim 23°$ (22–24°) and 43° (43–44°) ($\lambda_{CuK\alpha}$=1.54 Å), which are ascribed to the corresponding (002) and (100) crystallographic planes of graphite (see Fig. 3 *b*).[85] The average distance between the graphene-like layers varies from 0.347 (Ref. 135) to 0.443 nm (Ref. 136) depending on the type of precursor and carbonization temperature. The most common values are 0.37–0.38 nm.

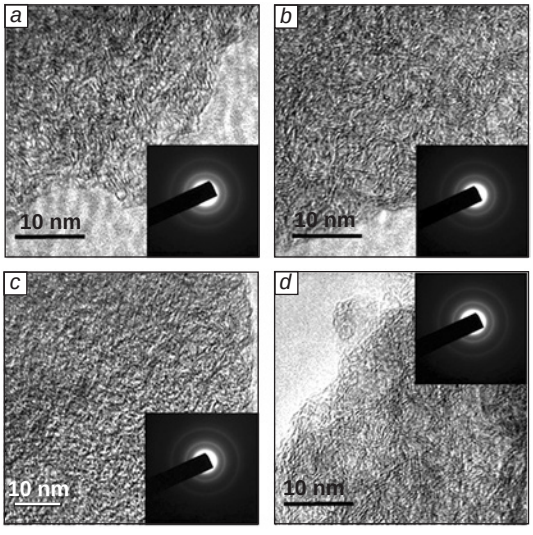

Figure 6. TEM images of a sample of hard carbon derived from mangosteen shell carbonized at 800 °C (*a*), 1300 °C (*b*), 1500 °C (*c*), 1600 °C (*d*).

It is noteworthy that some papers[39,65,137] reported a 'bell-shaped' dependence of the interlayer distance on the annealing temperature: an increase was observed with an increase in temperature from ~800 to 1250 °C[39] and a decrease with a further increase in temperature, which may indicate the existence of an 'intermediate', more disordered state.

Li *et al*.[33] and Xiao *et al*.[34] studied the influence of other carbonization parameters (in addition to the carbonization temperature) on hard carbon structural properties. More ordered structures were observed at slower heating rate.[34] Additional microwave treatment of hard carbon after its annealing leds to an increase in the length of carbon domains to almost 15 nm, while without additional microwave treatment this parameter did not exceed 5 nm.[33]

Since the strong broadening of reflexes in X-ray powder diffraction patterns provides only a rough estimation of the structure of hard carbon, the pair distribution function method is used for a more in-depth study. The atomic structure of hard carbon, its defects and the mechanisms of interaction of metal ions with the material are studied using synchrotron X-ray and neutron total scattering data.[33,80,114,138–142] The relevance of this method for hard carbon is due to the nanometer dimensions of graphitic (graphite-like) domains (crystallites), which violates the assumption of the presence of a long-range order in the crystal lattice, and to local defects in the atomic structure. The pair distribution function describes the atomic structure around a selected atom by the probability of finding another atom at a given distance from it. The graph of the pair distribution function $G(r)$ contains peaks at a distance r from the conditionally central atom, which are caused by the corresponding atoms in the material structure (Fig. 7).

The position of the maxima determines the interatomic distance. The intensity of each peak reflects the relative 'contribution' of atoms in the corresponding interatomic distance. The width of the peaks is related to the factors that can cause changes in the interatomic distances, primarily thermal fluctuations of the atoms.[114] The distances r determined in hard carbon using PDF correspond to different distances of the hexagons of graphene sheets.[114,138–140] In this case, as noted by the authors of papers,[103,135] the peak at a distance of 3.35–3.45 Å, corresponding to carbon atoms in adjacent graphite sheets, is practically absent regardless of the annealing temperature (it should be noted that its intensity is quite low in the case of graphite).[114,138] At higher annealing temperatures, the peaks in the $G(r)$ graph become narrower, indicating a greater ordering of the atomic structure.

Kubota *et al*.[130] showed that the maxima on the $G(r)$ plot at values of r greater than 3 Å for hard carbon differ in position and intensity from graphite. This may be due to the non-parallel arrangement of individual layers in hard carbon, defects at their edges, as well as the curvature of the layers, which in turn may be associated with a some of 5- and 7-membered carbon rings and other factors.[114,138–141]

The degree of ordering, or graphitization of hard carbon is estimated from Raman spectroscopy data.[32,55,60,116,118,120,121,121,129,143] There are several approaches to estimating the degree of graphitization. They are based on the study of D and G bands, which are characteristic of carbon materials with different microstructure and degree of ordering. The G band is observed at a frequency of ~1580–1600 cm^{-1} and is caused by in-plane vibrations of sp^2 carbon atoms in six-

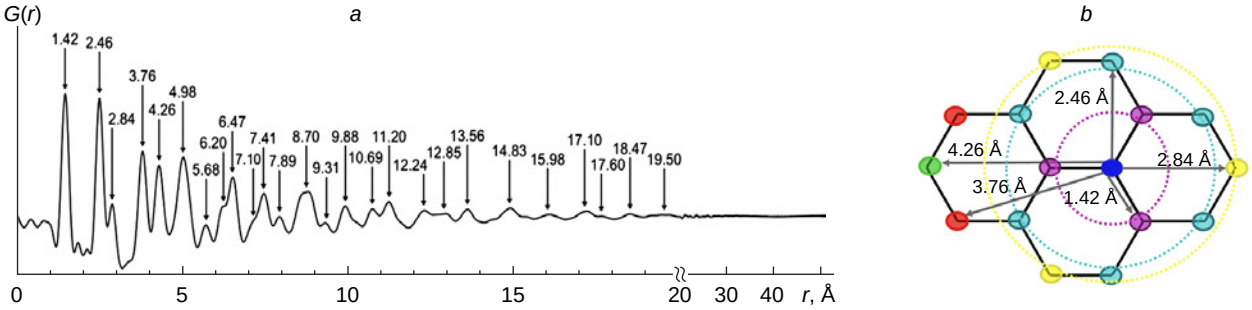

Figure 7. (*a*) Graph of the pair distribution function for hard carbon,[141] (*b*) schematic image based on paired distribution function data, showing the nearest neighborhood of the central atom in the graphene layer.

membered carbon rings (the E_{2g} mode of the irreducible representation of the D_{6h} group).[144,145] At ~1350–1360 cm^{-1}, the D band (D1) is observed, which is not characteristic of ideal graphitic lattice.[146] Its nature is the subject of long scientific debate. The D band has been associated with defects at the edges and inside graphitic planes (A_{g1} mode),[145] with symmetric stretching vibrations of six-membered aromatic rings,[128] or with double-resonant Raman scattering on carbon layers.[147] Raman bands and vibrational modes for carbon black and graphite are discussed in detail in a study.[145] The characteristic Raman spectrum of hard carbon is shown in Fig. 8.

Approaches assessing the degree of graphitization of a material are based on estimating the D1 : G ratio or the integral D3 : G ratio.[135] The D3 peak at 1500 cm^{-1} is observed for sp^3 carbon atoms in amorphous states,[145] so the second approach proposes to estimate the degree of graphitization by the ratio of sp^2- and sp^3-hybridized atoms. The first approach is the most common. The ratio is calculated from the peak heights or integral intensities signed as IG and ID (or AG and AD). The integral intensity ratio is calculated from the ratio of the areas under peaks G and D1 (IG/ID1). Gomez-Martin *et al.*[114] proposed to estimate the degree of graphitization by the calculation method (IG/(ID1 + IG)), which allows to obtain a value in the range from 0 to 1. The values of the ratio of the integral intensities D1/G for different samples of hard carbon are close and usually greater than 1. In addition, the width of the D and G peaks at half height decreases with increasing annealing temperature of the hard carbon samples, also indicating an increase in the ordering of the materials.[57,125]

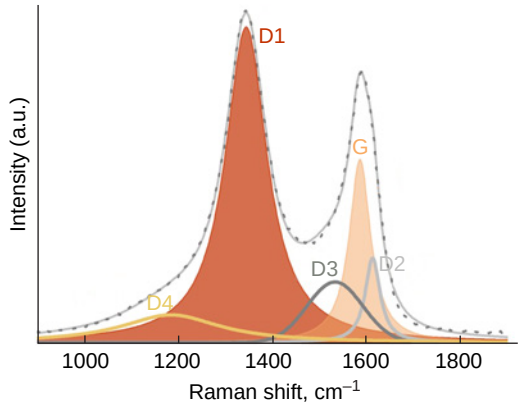

Figure 8. Raman spectrum of hard carbon and Gaussian approximation of peaks (the Figure was taken from authors archive to Ref. 73).

In addition to the presence of graphite-like domains, micropores were found in the microstructure of the samples (as visualized by TEM[91,122,127]), formed as a result of disordered stacking of nanoscale domains. A more detailed investigation of the porous structure of hard carbon is carried out using gas adsorption/desorption methods to study open pores and the SAXS method to study pores isolated from an external environment. Due to the small scattering angles, SAXS has a low resolution for single atoms and a high resolution for larger particles. The scattering coefficient of a particle is determined by the total electron density of the atoms within it, so the presence of regions of significantly different electron density in the sample (*e.g.*, closed micropores) will be reflected in the SAXS diffraction profile.[148] According to model representations, closed pores in hard carbon are spaces between graphite-like domains or separate graphene-like layers in the bulk. An example of the SAXS curve for hard carbon is shown in Fig. 3*d*. The part described as Q^{-4} on the plot of the reflection intensity *vs* the wave vector is associated with the reflection of X-rays from the surface of graphite-like particles.[112] The pores of hard carbon account for the appearance of convex regions on the curve (for a detailed model to interprete the SAXS curves for disordered carbon materials see[112]).

Several approaches have been proposed to determine the pore size of hard carbon.[63,130,132,149] For example, Simone *et al.*[132] used Guinier's dependence (1) to analyze the scattering intensity in the convex region:

$$I = N \cdot V^2 \cdot \exp\left(\frac{-Q^2 \cdot Rg^2}{3}\right) \quad (1)$$

where N is a pore number, V is the pore volume and Rg is radius of gyration.

Pore diameter (D_0) can be estimated using Eq. (2), a factor of 3/5 is introduced to account for the non-spherical oval-shaped[132] pores (see Fig. 3*a*):

$$Rg = \sqrt{\frac{3}{5}} \cdot \left(\frac{D_0}{2}\right) \quad (2)$$

Pore sizes of hard carbon derived from different precursors vary from ~0.6 to ~4.5 nm. Based on the SAXS data, it was found that the pore size increases with increasing annealing temperature.[63,127,130,132] At the same time, when the annealing temperature is increased from 700 to 1300 °C, the pycnometric density of the samples of hard carbon increases from 1.727 to 2.105 g cm^{-3}, whereas further increase of the temperature leads to a decrease of this parameter to 1.392 g cm^{-3} at 2000 °C (for comparison, the pycnometric density of graphite is 2.26 g cm^{-3}). Based on the analysis of the SAXS data and the determination of the skeletal (or effective) density (which is determined by the

total density of the skeleton and the closed pores) by helium pycnometry, it is assumed that this is due to an increase in the volume of closed pores with a simultaneous decrease in their number. This is explained by the formation of larger pores due to the merging of small ones.[127] It is also likely that closed pores can be formed due to the collapse of open pores as the annealing temperature of the material increases.[127]

The open pore portion in hard carbon is mainly determined by the gas adsorption/desorption method.[28,34,35,39,56–58,63,81,132,143,150–154] Nitrogen at 77.4 K is used to measure the specific surface area of the material (the ratio of the total surface area of the sample to its mass) and pore sizes larger than 0.7 nm,[40,127] CO_2 is used to measure pores smaller than 0.7 nm and, to account for their contribution to the specific surface area value, measurements are made at 273 K.[155] Measurements using N_2 and CO_2 can be complementary.[40,71,114] The reason for the differences in specific surface area values for the same sample of hard carbon when different gases are adsorbed thereon is related to the different sizes of their molecules,[114] and also to the fact that measurements with CO_2 at higher pressures (up to 10 kPa) allow the contribution of pores smaller than 0.7 nm, which are inaccessible to N_2, to be taken into account due to the better diffusion of carbon dioxide.[40,151]

There are at least 5 types of adsorption/desorption isotherms for gases that do not undergo chemisorption on the surface of the sample (Fig. 9). Type I isotherms are the feature of samples with micropores and relatively small surface areas, while types II and III are typical for macroporous and non-porous objects. Type IV and V isotherms are observed for mesoporous samples.[157] There is also the type VI isotherms, obtained for non-porous materials.[158] Type IV and V isotherms may have a hysteresis loop, which is interpreted when analyzing pore characteristics, such as their shape. There are a number of theoretical approaches and models for the analysis and calculation of material parameters which are discussed in detail in studies.[156,158–160] For hard carbon, different isotherms are obtained depending on the precursors, primary processing methods and annealing temperatures. For example, cork-derived samples are characterized by a combination of I and II type isotherms.[127] Materials from peanut shells and phenol formaldehyde resins have a combined I/IV type adsorption isotherm.[39,62] Type IV is characteristic of hard carbon from sodium polyacrylate[52] and some plant precursors, *e.g.*, *Ganoderma lucidum* residue.[117] Treatment of starting biomasses with hydrochloric acid can change the adsorption isotherm, *e.g.*, from type I to type II for argan samples, and from type III to type IV for typha[116] and peanut shell.[121]

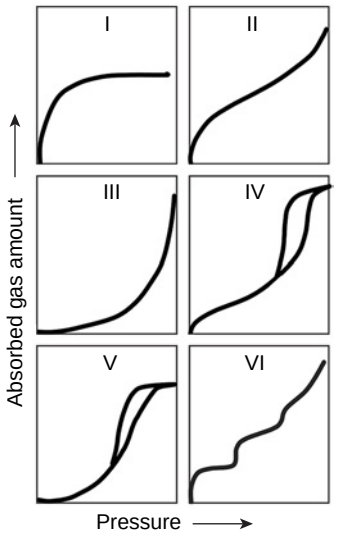

Figure 9. Gas adsorption/desorption isotherms on the adsorbate (see text for explanation).[156]

The Brunauer, Emmett and Teller (BET) equation is used in most works to describe the isotherms and calculate the specific surface area of the samples.[3,34,35,39–41,56–58,64,114,116,122,129,154,161] The specific surface area (SSA_{BET}) of hard carbons varies considerably depending on the precursor and can range from ~1 $m^2 g^{-1}$ (Ref. 132) to ~2500 $m^2 g^{-1}$ (Ref. 62) for different starting materials. The specific surface area of hard carbons derived from sugars, natural and synthetic polymers varies from several tens[34,161] to several hundreds of $m^2 g^{-1}$ (Ref. 62).

According to several studies,[58,63,122,125,127] increase in carbonization temperature from 800 °C (Refs 63, 122, 127) to 1600 °C (Refs 125, 127), leads to a decrease in the specific surface area of the samples, which may be related to the collapse of open pores.[127] For example, for hard carbon derived from phenol formaldehyde resin, SSA_{BET} decreases from 350 to 101 $m^2 g^{-1}$ with increasing carbonization temperature from 800 to 1500 °C.[39] It was shown[114,132] that at higher carbonization temperatures the specific surface area ceases to decrease significantly and can even slightly increase. In addition to the carbonization temperature, the argon flow rate over the samples during their high temperature carbonization has a significant effect on the specific surface area:[3] as the rate of Ar supply increases from 200 to 600 and 1000 $cm^3 min^{-1}$ respectively, a decrease in SSA_{BET} of hard carbon from sucrose is observed from 670 to 120 and 11 $m^2 g^{-1}$ respectively. This may be due to the faster removal of gaseous carbonization products, which can react with the carbon material, activating the surface and thus increasing the surface area of the samples. A high heating rate results in an increase in the specific surface area of hard carbon samples,[34] while a low heating rate of the samples contributes to a more effective desorption of gaseous products from the surface of the material during carbonization, thus reducing pore formation.

4.4. Study of defects

The main types of defects in hard carbon that can significantly affect its electrochemical performance are dangling bonds at the edges of graphite-like domains, vacancies within graphene-like layers, heteroatoms, atomic structure defects (due to the presence of sp^3 atoms in the material), *etc*.

The dangling bonds were studied by EPR spectroscopy.[130] Localized paramagnetic centers were attributed to dangling σ-bonds of carbon atoms at the edges of graphite-like domains and at the surface of open pores. The spectra showed a broadening of the peaks, which was explained by the presence of sp^3 carbon atoms in hard carbon, leading to a broadening of the energy gap between the valence and conduction bands. Using the EPR method, it was found that localized paramagnetic centres are able to interact with atmospheric oxygen, giving rise to a difference between the EPR spectra recorded in air and *in vacuo*.

Datta *et al.*[162] calculated the energy of vacancy formation in a graphene-like layer using the DFT method and showed that the formation of divacancies, *i.e*. two vacancies located at the adjacent points of the lattice, is energetically the most advantageous (the energy of monovacancy and divacancy formation is the same and is 8 eV, hence the removal of an atom in the first case requires 8 and 4 eV in the second case) (Fig. 10*a*). When divacancies are formed in the material, the

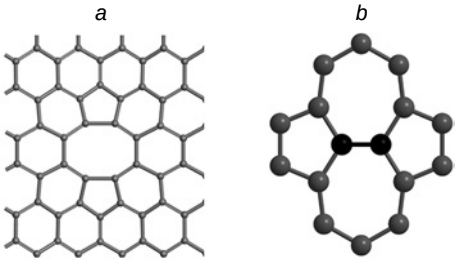

Figure 10. Schematic representation of defects in hard carbon: divacancies (*a*)[163] and Stone-Wales defects (*b*).[164]

atomic lattice remains virtually unchanged. According to calculations, in addition to divacancies, the formation of Stone-Wales defects is the most energetically favourable. They arise from rotations of C–C bonds by an angle of ~90° in the hexagonal structure (Fig. 10 *b*), resulting in two pentagonal and two heptagonal rings in the structure (their formation energy is 5 eV). At the same time, the dangling bonds are unstable in graphene-like layers.

The content of defects in the layer of sp^2 atoms can also be determined by evaluating the integral areas of the peaks in the PDF plot.[138]

Gomez-Martin *et al.*[114] proposed to estimate the degree of deformation of hard carbon β by Raman spectroscopy as 1 – α, where α is the degree of graphitization of the material. It decreases from 0.78 to 0.66 with increasing annealing temperature of hard carbon samples from 800 to 2000 °C [114] and from 0.76 to 0.65 with decreasing heating rate of samples from 5 to 0.5 deg min^{-1} (for annealing at 1300 °C).[34]

Defects in hard carbon can also be studied by measuring the active surface area, which is calculated from the chemisorption of oxygen. The amount of oxygen-containing complexes is determined by mass spectrometry from the amount of CO and CO_2 gases released during outgassing at 950 °C.[3,165] The active surface area depends on defects, such as vacancies and dangling bonds, as well as the presence of heteroatoms, adsorbed atoms and groups of atoms, *etc*. Zhang *et al.*[71] found that by increasing the annealing temperature from 950 to 1250 °C and decreasing the number of defects, the active surface area of hard carbon decreases from 23 to 1.1 $m^2\ g^{-1}$, at higher annealing temperatures further reduction of the active surface area is insignificant.

The defects in the layers and heteroatoms, which determine the value of the active surface area, can influence the ICE of hard carbon and the process of formation of passivation layers due to electrolyte decomposition. It was shown that as the active surface area decreases with increasing annealing temperature, there is initially a small growth in the ICE for anodes in sodium-ion half-cells from ~50–60 to ~70–75%, and then its decrease.[71] The mechanism of these changes requires further in-depth investigation. This may be due to the influence of other parameters of the material that are also determined by the annealing temperature, such as a reduction in the volume of open pores, the number of which affects the availability of the material surface for electrolyte decomposition. Defects and heteroatoms can also affect the electrochemical capacity of the material. For example, (C=O) groups can provide a reaction pathway for the reversible intercalation of Na, K and Li ions to form (C–O Na/K/Li).[166]

5. Electrochemical performance of hard carbon

Most of applied and fundamental studies and reviews are devoted to the electrochemical properties of hard carbon in SIBs, and to a much lesser extent in PIBs. As for LIBs, the practical interest to this material in this system is not very high today, mainly due to the more attractive properties of graphite, although it is often noted that hard carbon can be operated in LIBs at higher current densities and low temperatures.

The diversity of precursors and synthesis conditions mentioned above hampers the comparison of the electrochemical properties of hard carbons. Bommier *et al.*[30] gave a statistical analysis of the electrochemical characteristics for different carbon materials as a function of material type (graphite, graphitizable carbon, various samples of non-graphitizable carbon, *etc*.), charge-discharge current density and other parameters of the cycling process and suggested that there is a limit to the electrochemical capacity that can be achieved for hard carbon in SIBs. Theoretical calculations have shown that the theoretical capacity of hard carbon is in the range of 300–400 mA h g^{-1} for SIBs.[167] In practice, capacity values of around 300 mA h g^{-1} and higher have been achieved for samples of hard carbon derived from various precursors such as sucrose,[74,130,168] cellulose,[35,169] phenol formaldehyde resin,[42,134] biomass products.[170] Higher capacities (above 400 mA h g^{-1}) have also been reported, while the materials with such electrochemical properties are characterized by a high microporosity. The electrochemical performance of various samples of hard carbon in SIBs are given in Table 1.

The main factors affecting the electrochemical performance of hard carbon-based materials and the mechanisms underlying the electrochemical reactions of this material with alkali metal cations are discussed below.

5.1. Coulombic efficiency of hard carbon

Coulombic efficiency of the first charge-discharge cycle of anode material is a critical parameter that determines the mass ratio of the main components (cathode, anode and electrolyte) in metal-ion batteries. It is governed by intensity of irreversible processes, primarily, the formation of a passivation layer (or solid electrolyte interphase, SEI), responsible for the exclusion of a part of ions from the cycling process. SEI is formed through electrochemical decomposition of the electrolyte to produce a complex mixture of organic and inorganic compounds on the surface of the anode material. The composition, thickness, conductivity and chemical stability of the passivation layer depend on the electrolyte composition. This layer protects the electrolyte and the anode material from degradation and therefore influences the cycling stability.

The low ICE significantly complicates battery production: manufacturers are forced to use an excess of cathode weight in relation to the anode weight.[174] Another method of compensating irreversible capacity is the use of the so-called 'sacrificial' salt, a special additive to the cathode material that replenishes the lack of alkali metal cations after the first charge.[175,176] The carbon electrode can also be subjected to a preliminary electrochemical cycle in a half-cell with a metal counter electrode.For sodium-ion systems, the chemical 'presodiation' of anodes by contacting them with sodium metal or its salts [177–179] has been reported,with their subsequent utilization to assemble full cells.[180] However, the application of the last two methods in the battery production requires the addressing of

Table 1. Comparison of synthesis techniques from different precursors and electrochemical performance of hard carbon samples as anode material for SIBs.

Synthesis technique			Characteristics of sodium-ion half-cells				
			Anode material				
Precursor	Pretreatment method	Carbonization temperature, °C	Specific surface area, $m^2\ g^{-1}$	The 1st cycle discharge capacity, mA h g^{-1} (current density, mA g^{-1})	ICE (%)	Electrolyte	Ref.
Glucose	Caramelization in air at 200 °C	1300 °C in an argon flow	<1	300 (25)	89	1 M $NaPF_6$ EC : DEC 1 : 1	81
Glucose	Hydrothermal carbonization at 230 °C, filtration and drying of a solid	1500 °C in an argon flow	11	293 (30)	85	1 M $NaPF_6$ EC : DEC 1 : 1	86
		1700 °C in an argon flow	7	190 (30)	96		
Sucrose	Hydrothermal carbonization at 230 °C, filtration and drying of a solid	1300 °C in an argon flow	1.74	361 (20)	86	1 M $NaClO_4$ EC : DEC 1 : 1	34
Cellulose	Heating at 275 °C in air	1300 °C in an argon flow	506	353 (25)	94	1 M $NaPF_6$ PC	35
Cellulose	Hydrothermal carbonization at 200 °C, separation of supernatant and drying	1300 °C in an argon flow	10	302 (30)	91	1 M $NaClO_4$ EC : DEC 1 : 1	77
Pitch	Pretreatment at 300 °C in air	1400 °C in an argon flow	–	300.6 (30)	88.6	1 M $NaPF_6$ EC : DEC 1 : 1	37
Phenol formaldehyde resin	Resin synthesis (resol, formalin, maleic acid), carbonization at 800 °C in an argon flow	1500 °C in an argon flow	84.6	386 (10)	85	1 M $NaPF_6$ EC : DEC 1 : 1	42
Resin	Resin synthesis (phloroglucinol, glyoxylic acid, triethylenediamine) at room temperature, isolation and drying of a solid	1500 °C in an argon flow	3.5	294 (~7)	92	1 M $NaPF_6$ EC : DEC 1 : 1	153
Resorcinol formaldehyde resin	Resin synthesis (resorcinol, formaldehyde) at 40 °C	1600 °C in an argon flow	3.8	350 (20)	92	0.8 M $NaClO_4$ EC : DEC 1 : 1	171
Epoxy resin	Resin synthesis (Epoxy phenol novolac resin and maleic anhydride) at 180 °C, carbonization at 500 °C in an argon flow	1800 °C in an argon flow	1.43	480.3 (50)	84.6	1 M $NaPF_6$ DME	38
Magnesium gluconate + glucose	Precarbonization of the mixture at 600 °C, treatment with hydrochloric acid, drying of a solid	1500 °C in an argon flow	681	478 (25)	88	1 M $NaPF_6$ EC : DEC 1 : 1	92
Sosnowskyi hogweed	Heating at 200 °C in air, treatment with hydrochloric acid	1300 °C in an argon flow	7	221 (25)	87	1 M $NaPF_6$ EC : DEC 1 : 1	69
Hazelnut shell	Washing with hydrochloric acid	1400 °C in an argon flow	–	342 (20)	91.2	1 M $NaPF_6$ EC : DEC 1 : 1	84
Sucrose, egg-shell membrane, graphite	Egg-shell membrane pressed between pressed graphite plates	1300 °C in an argon flow	–	310 (20)	89	1 M $NaClO_4$ EC : DEC 1 : 1	172
	Hydrothermal carbonization of sucrose at 180 °C, then the solid product is mixed with graphite powder and pressed between graphite blocks	1300 °C in an argon flow	–	301 (20)	91	1 M $NaClO_4$ EC : DEC 1 : 1	172
Egg-shell membrane, graphite	Egg-shell membrane pressed between pressed graphite plates, pretreatment at 380 °C for 36 h	1300 °C in an argon flow	3.61	321.7 (20)	99.5	1 M $NaClO_4$ EC : DEC 1 : 1	173

Notes. EC is ethylene carbonate, DEC is diethyl carbonate, DMC is dimethyl carbonate, DME is dimethoxyethane, PC is propylene carbonate.

serious technological and engineering challenges due to the complexity of the operations performed on an industrial scale.

Chemical 'prepotassiation' is also known for potassium-ion systems. Prepotassiation is achieved by electrochemical pre-cycling of anode materials in a potassium-ion half-cell and further assembly of full cells with the treated electrode. Patent [181] proposes a method of treating finished electrodes with a mixture of naphthalene and potassium dissolved in an organic solvent. However, these approaches have not been scaled-up.

The main factors affecting the Coulombic efficiency of hard carbon in metal-ion batteries are:

1) electrode composition (which typically includes binder and various conductive additives, such as carbon black);

2) electrolyte composition;

3) material properties (specific surface area, defectiveness, presence and the type of heteroatoms).

5.1.1. Coulombic efficiency of hard carbon in SIBs

For hard carbon electrodes in sodium-ion electrochemical systems, the ICE can vary over a wide range. A number of articles have reported an increase in the ICE for hard carbon electrodes in sodium-ion cells when using materials with a specific surface area of less than 10 $m^2\ g^{-1}$.[34,182]

The influence of the anode composition in SIBs on the ICE has been studied in a number of works.[134,135,171,183–185] Bommier and Ji [186] showed that the fabrication of hard carbon electrodes without the addition of acetylene black helps to avoid decomposition of the electrolyte on the extended surface of this conductive additive, resulting in anodes having higher ICEs. The formation and optimization of a conductive carbon coating on hard carbon particles have been reported, with such composites showing ICEs above 70%.[184,185] This is attributed to the fact that a special conductive coating reduces the specific surface area of the material (from 95 to 70 $m^2\ g^{-1}$ for the coated sample).[184] High Coulombic efficiencies are also achieved in self-supported 'monolithic' electrodes prepared in the form of a polymer binder-free finished carbon film.[171,183] The authors explain this observation by the absence of significant grinding of the components of the electrode mixture,[134,187] whereas the preparation of traditional electrode slurry may increase the specific surface of the material due to the fragmentation of its components. At the same time, Bobyleva *et al*.[81] showed that even after milling, hard carbon with a monolith-like morphology (a monolithic carbon rod is formed during synthesis, and requires additional milling to be powdered) maintains high Coulombic efficiencies of about 89%. Some authors have demonstrated a significant increase in ICEs (up to 99.5%) by using a graphite plate as a template for the synthesis of hard carbon.[172,173]

The composition of electrolytes, *i.e*., salts and solvents, determines the composition of the passivation layer formed on the surface of the hard carbon as the electrolyte decomposes.

Typical electrolytes for hard carbon anodes are solutions of salts in non-aqueous organic solvents, such as alkyl carbonates and ethers.[186,188,189] For sodium ion systems, the salts of choice are perchlorate ($NaClO_4$), hexafluorophosphate ($NaPF_6$) or sodium bis(trifluoro)sulfonylimide ($NaN(CF_3SO_2)_2$, NaTFSI), sodium bis(trifluoro)sulfonylamide ($NaN(SO_2F)_2$) and others. Among the organic alkyl carbonates, the common solvents are ethylene carbonate (EC), propylene carbonate (PC) and their binary mixtures, as well as binary mixtures of EC with diethyl carbonate (DEC) and dimethyl carbonate (DMC), and other combinations. Among organic ethers, the most demanded are glymes — ethylene glycol dimethyl ethers with the general formula $CH_3O(C_2H_4O)_nCH_3$ ($n = 1–4$).

The electrochemical properties of hard carbon in electrolytes based on the two classes of the above solvents, namely, esters (EC, PC, DEC, DMC) and ethers (glymes), were studied in a recent works.[190,191] The use of glymes improves the cyclic stability and increases the Coulombic efficiency, which is associated with the formation of a thinner and more stable passivation layer (referred to as 'pseudo-SEI'). At the same time, it has been reported that the use of glymes for hard carbon is characterized by the phenomenon of 'co-intercalation', *i.e*. the intercalation of sodium ions surrounded by a solvate shell into the interlayer spacing.[192]

A number of studies have reported a beneficial effect of the fluoroethylene carbonate (FEC) electrolyte additive on the resulting passivation layer, reducing the degradation of anode materials during cycling in both sodium-ion half cells and sodium-ion full cells. However, the negative impact of this additive on the electrochemical performance of hard carbon also has been noted.[168,193] The observed negative effect may be related to the formation of a less electrically conductive passivation layer when FEC is added to the electrolyte.

One of the reasons why it is difficult to analyze and systematize data on electrolytes is the lack of a commercially available electrolyte that can be used as a benchmark. Hosaka *et al*.[194] noted that the differences in the quality of the salt, especially $NaPF_6$, and differences in the purity of the solvent significantly affect the properties of the finished electrolyte. The use of $NaClO_4$ is limited by its thermal instability, and application of NaTFSI is hampered by its ability to react with aluminium current collector.[188]

In addition to the use of various additives in the electrolyte, its properties can be modified by varying the salt : solvent ratio. Thus, the use of medium (2.5–3 M) and high (>3 M) concentrated solutions instead of the standard 1 M salt solutions ($NaPF_6$, NaFSA) improves the Coulombic efficiency of hard carbon anodes in SIBs, since it has been shown that increasing the concentration of the solutions contributes to the formation of a more stable passivation layer.[195–197]

Among the less common salts and solvents, sodium tetraphenylborate was found to increase the Coulombic efficiency to 95%;[198] also sodium bis(oxalato)borate in triethyl phosphate featuring high stability of the electrolyte to thermal decomposition.[199,200] The ability to operate at high current densities (charging within 5 min) was demonstrated by a system with a solid electrolyte based on sodium carborane $Na(CB_9H_{10})_{0.7}(CB_{11}H_{12})_{0.3}$.[201]

The electrolyte composition also has a significant impact on the cycling performance of hard carbon in full cells. For example, a full cell with $Na_3V_2(PO_4)_2F_3$ cathode and hard carbon anode retains 80% of its original capacity after cycling for 12 months in an electrolyte based on 1.5 M $NaPF_6$ in ethylene carbonate.[202] The authors noted that the use of electrolytes based on cyclic carbonates is preferable to maintain capacity during long-term cycling. In a follow-up study,[203] the cycling performance was improved through the use of a number of additives in carbonate electrolytes (vinylene carbonate, 1,3-propanesultone, succinonitrile, sodium difluoro(oxalato) borate), which allowed to retain 89% of the original capacity after 60 cycles at 55 °C.

5.1.2. Coulombic efficiency of hard carbon in PIBs

Compared to the ICE of hard carbon anodes in SIBs, the Coulombic efficiency of PIBs is significantly lower.

Similar to SIBs, PIB electrolytes typically comprise organic solvents (alkyl carbonates or ethers) and potassium salts. The latter are potassium hexafluorophosphate (KPF_6) or bis(trifluoro) sulfonylimide ($KN(CF_3SO_2)_2$, KTFSI).[194]

The Coulombic efficiencies of negative electrodes in such electrolytes is usually 40–65%.[204–209] Katorova *et al*.[205] studied the influence of the concentration of KPF_6 in diethylene glycol dimethyl ether (diglym) on the electrochemical performance of hard carbon anodes. It was shown that as the salt concentration increases from 1 to 2.5 M, the Coulombic efficiency increases from 70 to 77%. Dai *et al*.[206] compared two electrolyte solutions containing 1 M KPF_6, the first based on dimethoxyethane and the second based on the EC–DEC mixture. In the first case, the Coulombic efficiency was 77.3%, in the second case it was less than 50%. In addition, the dimethoxyethane-based electrolyte had a higher capacity, stable long-term cycling performance and the ability to operate at high current densities. For example, in the dimethoxyethane-based electrolyte at a current density that allows charging or discharging in 3 minutes (denoted as 20C), the capacity of hard carbon was 112 mA h g^{-1}, and in a mixture of ethylene carbonate and diethyl carbonate this value was 11.9 mA h g^{-1}.

As for the salts for electrolytes, the Coulombic efficiency of hard carbon anodes in potassium-ion half-cells with dimethoxyethane electrolyte was 76.3% in the case of 1 M KPF_6 and 44.8% in the case of 1 M KTFSI.[207] However, in alkyl carbonate solutions it is close for both salts, just over 50%. Thus, a higher Coulombic efficiency in ether-based electrolytes can be assumed as a general trend.

5.2. Capacity and operating potential of hard-carbon anodes

The capacity and operating voltage of anodes are usually estimated based on their galvanostatic measurements in half cells, where the counter electrode is an alkali metal electrode as an 'infinite' source of corresponding ions.

5.2.1. Capacity and operating potential of hard-carbon anodes in SIBs

A typical galvanostatic charge curve for hard carbon in a half cell with a sodium counter electrode can be divided into two distinct regions, a sloping region up to ~100 mV *vs* Na/Na^+ and the subsequent more flat region (termed as a plateau, quasi-plateau or pseudo-plateau) from ~100 to 0 mV (Fig. 11 *a*). Capacity values for both regions are usually analyzed in terms of being affected by material properties such as interplanar distance d_{002}, ordering, specific surface area, porosity, defectiveness and the presence and composition of heteroatoms (*e.g.*, O, N).

The interlayer distance is one of the key parameters in the study of the mechanisms of electrochemical reversible intercalation of metal ions into the microstructure of the material. For sodium-ion electrochemical systems, there is an increase in the plateau region and a decrease in the sloping region of the galvanostatic curves with a decrease in the distance d_{002} and an increase in the lateral dimensions of the graphite-like domains, observed when raising the annealing temperature of the samples, *i.e*. with a greater degree of graphitization of the material. As already mentioned, in sodium-ion half-cells the maximum capacity of hard-carbon anodes is observed for materials obtained by annealing at 1300–1500 °C. Increasing the annealing temperature above these values decreases the anode capacity. This can be due to an increase in the degree of graphitization and growth in the size of graphite-like domains (as mentioned above, reversible intercalation of sodium ions into graphite is difficult, unlike lithium or potassium ions).

An important task is to elucidate the relationship between the porosity and pore size of a material and its key electrochemical properties such as capacity and Coulombic efficiency. Among the main parameters of the material that determine its capacity, the size and number of closed micropores are singled out. Metal ions are considered to be able to reversibly fill micropores of hard carbon through diffusion between carbon layers. As the annealing temperature increases (with increasing pore size, as determined by SAXS) a boost in capacity is observed in sodium-ion half-cells,[35,63,127,132] with a concomitant increase in capacity in the plateau region of the galvanostatic charge-discharge curve.[130]

For sodium-ion systems, a number of studies contained experimental data with the charge-discharge curves representing only a sloping region down to 0 V.[8,61,62] The tested samples of carbonaceous materials featured high specific surface area (above 1430 m^2 g^{-1}).[62] In this case, it was assumed that sodium cations interact with defects and heteroatoms on the material surface rather than with its internal volume. The charge curve in such cases is similar to that of graphitizable carbon, for which the intercalation mechanism of the interaction of sodium ions

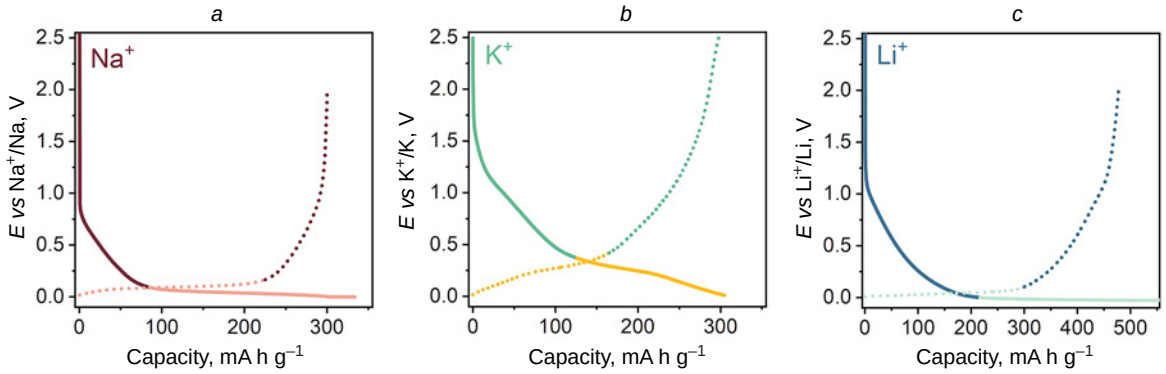

Figure 11. Typical galvanostatic charge-discharge curves of hard carbon in an electrochemical half-cell *vs* sodium metal (*a*), potassium metal (*b*), lithium metal (*c*) (the Figure was created by the authors using original data from the studies[73,81,130]). The charge curve is indicated by the solid line, the discharge curve is indicated by the dashed line. The division of the charge and discharge curves into two colours helps to explain its division into two regions (slope and plateau) described in the text.

with the material is being questioned by some authors.[30,185] However, it should be noted that the possibility of graphitization of the material was rarely tested in the works, so it is not always possible to clearly understand which type of carbon, graphitizable or non-graphitizable, was studied by the authors.

Non-graphitizable carbonaceous materials have been shown to be capable of long-term cycling stability. A number of papers have reported retention of more than 93% of capacity for 1000 charge-discharge cycles at a current density of 0.2 A g^{-1} (see [208]) and 73% of initial capacity for 10 000 cycles at 2 A g^{-1} (see [209]).

5.2.2. Capacity and operating potential of hard-carbon anodes in PIBs

In potassium-ion systems, two regions are also distinguished on the galvanostatic charge-discharge curves, a sloping region above 0.4 V *vs* K/K^+ and a plateau or quasi-plateau region below these values.[119,135,166] Other authors, *e.g.*, Kubota *et al.*[130] identified three sloping regions (Fig. 12) in the ranges of 0.002–0.2, 0.2–0.7, 0.7–2.0 V *vs* K^+/K.

The influence of the synthesis conditions and the microstructure of hard carbon on the capacity ratio for these regions has been explored in a number of papers. For example, it was shown that raising the annealing temperature during the synthesis of hard carbon from 1100 to 1500 °C increases the specific capacity of the anode material in all regions of the charge-discharge curve.[35,42] Kubota *et al.*[130] found that the specific capacity of anodes based on hard carbon samples carbonized at temperatures between 700 and 2000 °C does not change significantly over the whole range of potentials, but in the same time, there are changes in capacities of different regions of the galvanostatic curve. Thus, the capacity in the range of 0.7–2.0 V decreased drastically and the capacity in the range of 0.2–0.7 V increased. The capacity in the potential range of 0.002–0.2 V is significantly lower than in other potential ranges, and reaches its maximum of 47 mA h g^{-1} for the material carbonized at 1800 °C. The authors believe that the capacity of the samples carbonized at lower temperatures (700–900 °C) is mainly associated with the intercalation of potassium cations in the space between the defective graphene-like layers with a large d_{002} distance.

In a number of works devoted to PIBs, materials derived from different biomasses were studied.[120,143,210] For example, the capacity of ahard carbon anode material derived from corn husk was about 230 mA h g^{-1}, while after 100 cycles it retained 89.1% of the original capacity and was ~205 mA h g^{-1}.[120] The special feature of various biomasses is the presence of naturally occurring heteroatoms in the hard carbon; and such dopants have been specifically explored.[108,111,166,211] The analysis of the publications devoted to carbon doping does not allow to speak about a boost in capacity or the ICE for such anode materials. Moreover, virtually no quasi-plateau region was observed in galvanostatic curves at low potentials.[108,211] The predominance of pseudo-capacity interactions between hard carbon and potassium cations observed in these works is associated with an increase in the number of defects and interlayer space in hard carbon. On the other hand, it was noted [108,111,166,211] that the hard carbon doping with heteroatoms improves the capacity maintenance during long-term cycling and an increase in the anode capacity at high current densities.

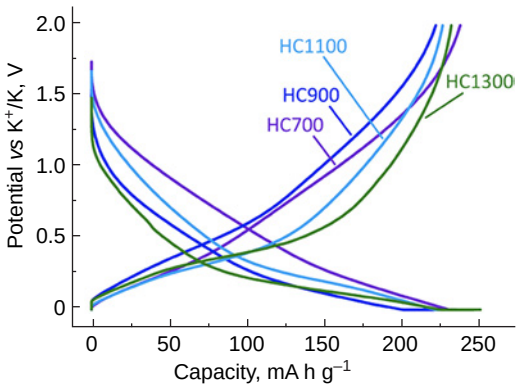

Figure 12. Galvanostatic curves of the hard carbon samples carbonized at different temperatures.[130]

5.2.3. Capacity and operating potential of hard-carbon anodes in LIBs

Due to the larger interlayer distance compared to graphite, faster diffusion of lithium ions is expected in hard carbon, leading to better operation at high current densities.[212] In addition, the microstructure of hard carbon allows additional storage of lithium ions in micropores below 0 V *vs* Li/Li^+ (see Fig. 11 *c*).[212–214] Therefore, some studies consider hard carbon as a safer and higher capacity alternative to graphite for the new generation of lithium-ion batteries.[215–218] For example, the prototype of LIBs based on the $LiNi_{0.6}Mn_{0.2}Co_{0.2}O_2$ cathode and the hard carbon anode showed good cycling stability at current densities providing charge or discharge for 20 min (designated as 3C).[218] At the same time, in the case of SIBs and PIBs, cycling stability is usually studied at current densities that provide charge or discharge in 1 h (designated as 1C). It was shown that increasing the current density above 1C in the SIB prototypes promotes the deposition of sodium metal.[219]

In addition to studying the relationship between the ratio of sloping and plateau capacities with synthesis conditions and material properties, the elucidation of mechanisms of the electrochemical processes occurring during the charge-discharge cycle remains relevant. Given the complexity of the subject under study, these mechanisms are still the matter of intense debate.

5.3. Interaction models for hard carbon and alkali metal ions in electrochemical cells

Based on the available experimental data, the main reaction pathways for the interaction with alkali metal cations can be distinguished:

1) interaction with defects and heteroatoms;
2) intercalation of ions into the interlayer space;
3) filling of open and closed micropores by metal ions, where the formation of metal clusters can be observed.

5.3.1. Interaction models for SIBs

Stevens and Dahn[220] were the first to study hard carbon as an anode material for SIBs in 2000. The D-glucose-derived material demonstrated a capacity of 300 mA h g^{-1}. The authors proposed a model of a two-step mechanism by which sodium cations intercalate into the microstructure of hard carbon. According to the authors, two processes occur during charge and discharge, each corresponding to its own part in the galvanostatic curve.[217] At the sloping region (above 100 mV), a shift of the peak

corresponding to the plane (002) towards smaller angles was detected by the *in situ* wide angle X-ray scattering. It was suggested that intercalation of metal ions into the interlayer space occurs at this site. According to the authors' model, after intercalation, in the range from 100 to 0 mV *vs* Na/Na^+, sodium metal deposites in the pores of the carbonaceous material. This model has been called 'house of cards' or 'intercalation–filling' (see Fig. 13 *a*); it is the model adopted by most authors exploring the electrochemical properties of hard carbon (see, *e.g.*, Ref. 15). A similar mechanism of interaction between hard carbon and alkali metal cations has been proposed by another scientific group.[221] In this study, hard carbon electrodes were charged to different degrees (a number of 'points' in the galvanostatic curve) in a half-cell *vs* sodium metal and studied by PXRD, SAXS and Raman spectroscopy. The combination of these methods showed that in the sloping region, the change in the position of the G line in the Raman spectra together with the shift of the peak (002) towards lower angles is associated with the intercalation of sodium ions into the interlayer space of hard carbon. The processes occurring in the plateau region were interpreted from the SAXS measurements, *i.e.* the drop in intensity in the region of 0.03–0.07 $Å^{-1}$ was ascribed to the filling of the hard carbon nanopores with sodium ions.

With the increased attention paid to SIBs, studies of the mechanisms of interaction of hard carbon with alkali metal cations have recently received a new impetus. The 'intercalation-filling' mechanism has received a number of additions and critical remarks, in particular because of the curve region below 100 mV, which is mainly associated with the deposition of sodium metal clusters inside micropores. This issue was studied by ^{23}Na NMR spectroscopy. In the studies,[222–223] the formation of metal clusters was not observed, although it was found that sodium ions occupy at least two different energy positions.

In 2012, Cao *et al.*[224] proposed a new model of a two-step 'adsorption–intercalation' mechanism (Fig. 13 *b*). According to the authors, based on cyclic voltammetry data, the sloping voltage curve corresponds to the reaction of sodium cations with the surface of graphite-like domains. At lower voltage, sodium ions are introduced into the interlayer space of hard carbon due to the large interlayer distance.

Subsequently, the 'adsorption–intercalation' model was confirmed by *ex situ* PXRD,[225] which showed that the shift of the peak corresponding to (002) reflection of the graphite structure occurs in the range of potentials below 0.2 V, while the interlayer distance increases from 3.96 to 4.16 Å for the charge in this region. Bommier *et al.*[138] supplemented this model by an assumption of the third stage of the mechanism of interaction of sodium ions with hard carbon at potentials close to 0 V *vs* Na/Na^+. The authors found that in the plateau region, the diffusion coefficient of sodium ions reached a minimum at a potential of 0.05 V, and its significant increase was observed with decreasing potential. Based on these findings, it was concluded that the deposition of sodium metal occurs in the range of 0.05–0.02 V, which corresponds to the third, more sloping voltage region.

Using on the above models, Zhang *et al.*[71] classified hard carbon materials into three groups according to the character of the galvanostatic curve in SIBs and the physical properties of the materials, which in turn depend on the annealing temperature. In the materials of the first group, obtained at temperatures below 950 °C, the energy storage mechanism is significantly influenced by the presence of oxygen- and nitrogen-containing functional groups, as well as by the strong defectiveness of the material. Sodium ions can interact both reversibly and irreversibly with functional groups of hard carbon obtained at temperatures below 950 °C. In materials of the second group, prepared at annealing temperatures of 950 to 1550 °C, the galvanostatic curve in sodium-ion systems is divided into two regions. According to the authors, the mechanism of storage, corresponding to the sloping region, is related to the interaction of sodium ions with defect sites presenting in graphite-like domains. Charge storage in the plateau region occurs *via* filling the micropores of the material with sodium ions. The third group of materials, synthesized at temperatures between 1550 and 2200 °C, do not show the plateau region. At the same time, according to the *in situ* XRD data, no shifts of the (002) reflection were detected, and therefore, the authors questioned the idea of intercalation of sodium ions into the interlayer spacing of the graphite-like domains. Based on these data, the third model of the two-step 'adsorption–filling' mechanism was proposed (Fig. 13 *c*). Li *et al.*[125] argued that this model is confirmed by the TEM results

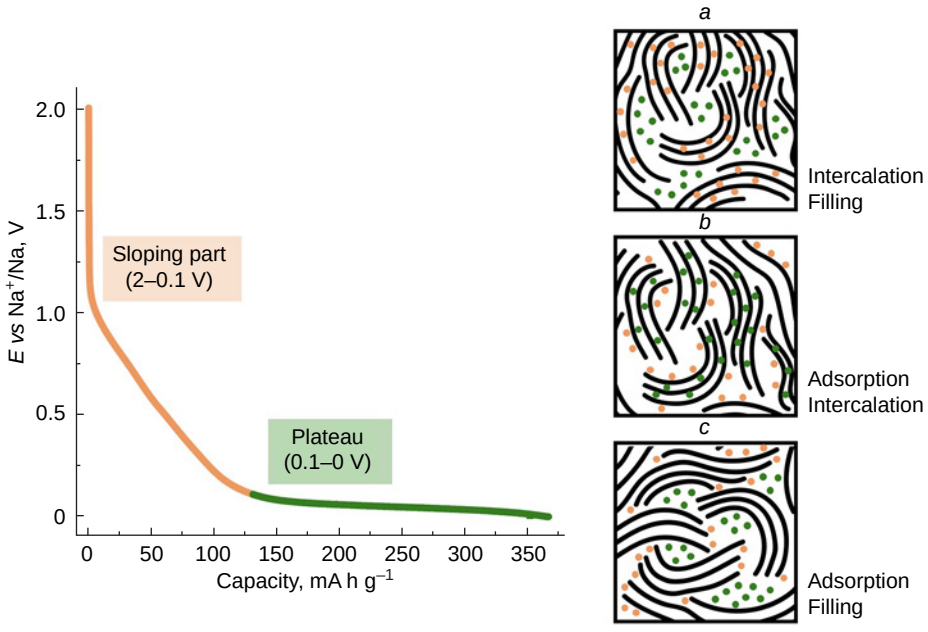

Figure 13. Models of two-stage mechanism of electrochemical interaction of sodium ions with hard carbon anode: 'intercalation–filling' (*a*); 'adsorption–intercalation' (*b*); 'adsorption–filling' (*c*). The Figure was created by the authors using original data from the studies.[71,221–226]

for the hard carbon material charged to 0 V. The authors have not found a change in the distance between graphene-like layers, but found a peak of sodium metal.

The fact that the sloping region of the charge-discharge curve is related to the processes of chemo- or adsorption of sodium ions onto the surface of the carbon particles, is supported by the disappearance of the plateau region and the retention of only the sloping region of the galvanostatic curve with an increase in the specific surface area and the formation of a large number of micropores open to the electrolyte.[74,227]

Samples of hard carbon doped with boron, phosphorus and sulfur atoms also demonstrated the change in electrochemical performance (elongation of different charge/discharge voltage regions).[102] The authors note that doping hard carbon with these heteroatoms increases the storage capacity of the sloping region. At the same time, the highest capacity is observed for B-doped carbon. Such an influence of heteroatoms on the capacity is due to the fact that their presence can increase the graphite interlayerdistance (in the case of S and P) and create more defects in the microstructure (N-, O- and B-doping).[228]

The electrochemical processes in the plateau region at the voltage range from 0.1 to 0 V in sodium-ion systems are also much discussed. It is the most important for SIBs because its length determines the energy storage capacity of the battery. The nature of the processes taking place at the anode at potentials close to 0 V has been studied by various methods, including NMR spectroscopy.

Grey's group[140] confirmed the hypothesis of metal cluster formation using *operando* ^{23}Na NMR measurements. Two sodium signals, 'ionic' at –40 ppm and 'metallic' at 760 ppm, were detected in the NMR spectra of the electrode in the charged state. During anode charging, the signal from the sodium involved in the charging process is shifted towards metallic sodium. The authors also hypothesized a high activity of charged electrodes in air, which could explain why the signal of sodium metal was not detected in previous *ex situ* NMR studies.[229] The importance of carrying out *operando* experiment was pointed out: in the *ex situ* experiment, *i.e*. after disassembly of the electrochemical cell, the hard carbon electrode degrades due to the high reactivity of the newly formed clusters. Morita *et al*.[149,230] used *ex situ* NMR to find out a correlation between the parameters of material synthesis and the nature of the Na signal in fully charged electrodes and concluded that metal clusters detected by NMR are formed in materials with large micropore radii of up to 1.95 nm, as determined from the SAXS curves, in contrast to materials with small pores (radius is 1.42 nm). The authors found that the pore size estimated from the SAXS data did not exhibit an evident correlation with the signal position of metal sodium clusters, which was determined by NMR. However, hard carbon samples obtained at higher carbonization temperatures (above 1600 °C) show a stronger signal shift towards metallic sodium. For the fully charged electrode from the material prepared at 2000 °C, the sodium signal is almost identical to that of metallic sodium.

Alvin *et al*.[135] proposed that the interaction of sodium ions with surface defects and functional groups is associated with a sloping voltage region up to 0.2 V, and the second part of the sloping region from 0.2 to 0.1 V appears due to adsorption of cations on the surface of the graphene-like layer. The intercalation of sodium ions into the interlayer spacing corresponds to the plateau voltage region. The authors also identified the fourth stage of the interaction process, which involves secondary filling of hard-to-reach closed pores at potentials close to 0 V.

The interaction of sodium ions with hard carbon has also been studied using small- and wide-angle X-ray scattering (SAXS and WAXS). In one of their first papers, Stevens and Dahn[217] used *in situ* SAXS measurements. In 2019, a group led by Yamada[231] used detailed analysis of *ex situ* WAXS data acquired during plateau charging of hard carbons with different degrees of ordering to reveal the appearance of a new peak (at $Q \approx 2.0-2.1$ Å^{-1}, with $d \approx 3.7$ Å,) close to the peak corresponding to the reflection of the 002 structure of graphite (at $2\theta = 23-25°$, $Q \approx 1.6-1.8$ Å^{-1}). Based on theoretical calculations, models of metallic sodium clusters have been proposed for this new peak. Another research group[183] attributes the appearance of a new peak to the formation of sodium intercalates. In addition to the XRD measurements, the formation of metal clusters in the plateau region was investigated by Raman spectroscopy.[232–234] It was shown that during charging of hard carbon, the G-band signal is not shifted in the plateau region, as would be expected in the case of intercalation. At the same time, a shift from 1600 to 1560 cm^{-1} is observed in the sloping region above 100 mV[233] as indicating the probable formation of intercalates.

It should be noted that the interpretation of PXRD and Raman spectroscopy data for disordered materials is somewhat difficult. For example, the peak corresponding to the (002) reflection of the graphite structure in hard carbon is significantly broadened, and the typical Raman spectrum of amorphous carbon show other bands in addition to the D1 and G bands.[235]

The charge-discharge process for hard carbon anodes in sodium-ion cells has also been explored by PDF.[114,130,138,139] Gomez-Martin *et al*.[114] found that the capacity of the sloping region of the electrochemical charge-discharge curve decreases monotonically with increasing annealing temperature, which is in line with a decrease in defect concentration and an increase in the size of graphite-like domains. In turn, the plateau region capacity reaches its maximum at the annealing temperature of 1400 °C. The maximum interplanar distance in graphite-like domains determined by PDF corresponds to the same temperature. The correlation of the interplanar distances and defect concentrations with the capacity of each section of the galvanostatic curve led the authors to the conclusion that the interaction followed the 'adsorption-intercalation' mechanism. On the other hand, Kubota *et al*.[130] considered the mechanism of interaction of sodium ions with hard carbon according to the 'intercalation-adsorption' model, and they also found that as the annealing temperature is increased up to 2000 °C, the capacity continues to rise monotonically in the plateau region. Interestingly, this trend was not observed when interacting with lithium and potassium ions. For these systems, the authors proposed a three-step model, in which metal ions first interact with defects on the surface of graphite-like domains, followed by intercalation into the interlayer spacing, and near 0 V begin to fill micropores to form metal clusters.

Bobyleva *et al*.[216] confirmed a three-stage model similar to that presented in a study[138] by exploring the pseudocapacitive (surface-controlled) properties of materials with different textural characteristics using linear voltammetry. The authors concluded that the sloping voltage region corresponds to pseudocapacitive processes and the plateau region corresponds to intercalation. It was also suggested that there was a third stage corresponding to the filling of closed pores of hard carbon with sodium ions.

In 2020, an extended version of the mechanism of interaction of sodium ions with hard carbon was presented. Based on the *ex situ*[23] Na NMR measurements, small-angle neutron scattering

and PDF in combination with theoretical calculations, it suggests that the sloping region corresponds to several processes at once, including not only interactions with the surface and defects (all types of the above defects), but also intercalation into the interlayer spacing.[86]

An important publication in the study of the mechanism of sodium ion insertion was the result of the collaborative survey of the research groups of Allan and Grey,[141] who used a combination of *operando* ^{23}Na NMR and *operando* PDF and showed that the size of the metal clusters does not exceed 13–15 Å regardless of the pores radii in the material. The authors also noted that the intercalation of sodium ions in the interlayer spacing can occur due to the presence of five- and seven-membered rings in the microstructure of hard carbon.

Surta *et al*.[236] modelled the microstructure of hard carbon samples using PDF results from neutron scattering. The authors put forward a fundamentally new hypothesis that sodium ions interact mainly with specific defects in the microstructure of hard carbon. One of these defects is thought to be the most curved regions of the graphene-like layer.

5.3.2. Interaction models for PIBs

Studying the interaction between potassium ions and hard carbon by cyclic voltammetry (CV), galvanostatic intermittent titration technique, *ex situ* and *in situ* Raman spectroscopy,[211,237,238] resulted in a conclusion about different interaction ways between potassium cations and hard carbon in the sloping and plateau regions. The sloping region was attributed to a pseudo-capacitive processes caused by the interaction of K^+ ions with defects, including heteroatoms. The plateau region was assigned to intercalation. Based on the calculation of the density of states, Alvin *et al*.[237] proposed a model for the intercalation of K^+ ions between carbon layers, according to which potassium cations tend to form ordered structures. In this case, the potassium atoms are located directly under the carbon atoms in the intercalates. Such intercalates are unstable. Kubota *et al*.[130] also assumes the formation of ordered intercalates of graphite with potassium cations.

Chen *et al*.[119] suggested a slightly different mechanism of electrochemical interaction of K^+ ions with hard carbon. It is based on an in-depth analysis of the CV measurements, the shift of the X-ray diffraction peak at $2\theta \sim 23°$ towards smaller angles during anode charging and back again during discharging, the reversible appearance of the K 2p peak in XPS spectra and the simultaneous reversible decrease of the carbon C1s peak for charged/discharged anode, the analysis of data from galvanostatic intermittent titration, in which it was found that the diffusion coefficient of potassium cations is significantly higher in the potential range > 0.4 V (in a study,[237] the limit of the 0.3 V potential range is indicated as 0.3 V). Taken together, these data let the authors to conclude that the sloping region corresponds mainly to pseudo-capacitive processes (associated with sorption) and the plateau region corresponds to diffusion. However, according to the authors, these processes cannot be completely separated. Firstly, adsorption takes place at surface active sites and in the hard carbon pores, and at the same time, a some intercalation of potassium cations begins (sloping voltage region). After the hard carbon pores are filled with potassium, the potential drops to ~0.4 V and the previously adsorbed potassium cations intercalate between the layers of the hard carbon (plateau region) with simultaneous absorption of new potassium cations on the vacated pores.

A new approach to modelling the mechanisms of electrochemical interaction of K^+ ions with hard carbon was proposed based on CV measurements, galvanostatic intermittent titration, *ex situ* X-ray diffraction data and *in situ* Raman spectroscopy.[239–241] The authors relate the mechanism of interaction to the carbonaceous microstructure and offer several models depending on the annealing temperature of hard carbon. It is noteworthy that this approach has much in common with the reported mechanism of interaction of hard carbon with sodium ions.[86] The amorphous component of hard carbon[239] stipulates adsorption of potassium cations, while graphite-like domains cause intercalation. Thus, for materials with a high proportion of amorphous component annealed at low temperatures of 800–1000 °C, the mechanism of interaction with K^+ ions is adsorptive. In this case only a sloping region is observed on the charge-discharge curves. For the materials annealed at T = 1000–1500 °C, the galvanostatic curve shows a sloping region and a plateau region at a potential < 0.4 V, leading the authors to suggest an adsorption–intercalation mechanism of interaction of K^+ ions with hard carbon. For the most ordered samples annealed at T = 1800–2900 °C, intercalation processes contribute most to the interaction with K^+ ions. In this case, the charge-discharge curves reveal longer low-voltage plateau.

Lin *et al*.[241] suggested the adsorption mechanism of interaction with K^+ ions both for low-temperature samples and for samples annealed in the temperature range of 1000–2000 °C. In the first case, the adsorption takes place on the defects of disordered structures and heteroatoms and moieties containing them, and in the second case, the adsorption sites are ordered carbon layers forming domains. The intercalation mechanism of interaction of K^+ ions with hard carbon is proposed for materials annealed at temperatures above 2000 °C.

In all these studies, the of K^+ ion storage mechanisms in hard carbon are determined by adsorption and intercalation processes. In case of PIBs, energy storage as a result of filling the pores of the material with metal cations in the case, in contrast to SIBs, is a controversial issue,[239,242] since to date there are no data unequivocally confirming this mechanism. Li *et al*.[240] suggest that nanopores of about 0.5 nm may act as adsorption sites for potassium ions, which have a size of 0.38 nm in the solvated state. Huang *et al*.[243] proposed a qualitatively different mechanism of potassium cation storage in hard carbon. The authors associate the sloping region with potassium adsorption on heteroatoms and defects, and the plateau region with pore filling. Using the CO_2 adsorption/desorption method, the average pore size is estimated to be 0.5 nm. This value is smaller than the interplanar spacing of graphite with potassium cations intercalated therein (0.53 nm). Accordingly, the authors suggest that potassium cations fill the pores to form ordered structures similar to the potassium intercalation in graphite.

Further development of models for the potassium, and possibly sodium, cationstorage in hard carbon, can be based on the ability of these cations to form adducts with molecules of aromatic hydrocarbons containing curved planes due to the presence of five-membered rings. This ability of potassium cations to interact with corannulene has been reported.[244–246]

Therefore, the storage mechanism of alkali metal cations in hard carbon is multi-stage and depends largely on the hard carbon microstructure. The microstructure of hard carbon is in turn determined by the method of preparation, *i.e*., annealing temperature, method of pre- and post-treatment, type of precursor. The most important parameters of the microstructure include the average interlayer distance, micropores radius, defects, presence of heteroatoms. In the above publications, the

authors demonstrated the ability of alkali metal ions to penetrate into the interlayer spacing of hard carbon, interact with various defects and heteroatoms, and fill micropores to form metal clusters. The most contradictory point is the essential difference between the proposed models of K^+ cation storage in hard carbon. However, this contradiction can be explained by the fact that the term 'hard' covers a variety of materials with different microstructures. Nevertheless, the determination of the exact nature of the relationship between the parameters of the material and its electrochemical properties remains an urgent task that requires the explanation of a series of experimental data.

6. Conclusion

In this review, the main research findings of the properties of hard carbon obtained under different synthesis conditions and the electrochemical performance of hard carbon anode for metal-ion batteries are discussed in detail.

The hard carbon microstructure implies several different reaction ways for interaction with alkali metal ions. Establishing the dependence of material parameters (presence of defects, interlayer distances, pore size, *etc*.) on synthesis conditions (nature of precursors, methods of their processing, annealing temperature, *etc*.) as well as correlations of the mechanism of interaction between hard carbon and cations of different metals with the physicochemical properties of the material remain relevant.

Currently, for hard carbon in SIBs, the average specific capacity is about 300 mA h g^{-1} and the ICE is ~90%, while in PIBs, the average specific capacity is about 250 mA h g^{-1} and the ICE is ~50%.

Graphite is still a benchmark carbon material used as an anode material for metal-ion batteries (since in the most developed technology of LIB production, its specific capacity is about 370 mA h g^{-1}, ICE is over 95%, cycling stability is high). Developers of other carbon anodes suitable for SIBs and PIBs are targeting such electrochemical properties. The progress of recent years and the fundamental properties (reversible capacity, cycling stability, Coulombic efficiency) of hard carbon suggest that similar electrochemical performance can be achieved for it in SIBs in the near future. The development of technology for the production of hard carbon and anodes based thereon for PIBs will probably require more significant efforts.

In addition, the prospect for further increasing the capacity of anode materials for sodium and potassium ion batteries is the design of composites containing antimony, tin, lead and bismuth (similar to the graphite/silicon pair), as well as the creation of materials containing a deposited alkali metal.[247] The use of carbon black as a material for negative electrodes in SIBs and LIBs is also reported.[96]

Although hard carbon is the most promising anode material for sodium-ion and potassium-ion batteries, there is currently no consensus in the scientific community on the optimal methods for producing it, reliable methods of studying it, or the mechanisms of its operation. Over the last few decades, there have been significant breakthroughs in the study and understanding of the peculiarities of this material, but so far the data, observations and regularities obtained using different methods on different samples often contradict each other. It is obvious that further development of the SIBs and PIBs will require a more thorough, detailed and methodical study of hard carbon.

This review was financially supported by the Russian Science Foundation (Project No. 17-73-30006). The authors are grateful to G.P. Lakienko and M.A. Novikov for their help in preparing illustrations.

7. List of abbreviations and designations

AFM — atomic force microscopy;
BET — Brunauer–Emmet–Teller equation;
CV — cyclic voltammetry;
DEC — diethyl carbonate;
DMC — dimethyl carbonate;
EC — ethylene carbonate;
EDS (EDX) — X-ray energy dispersive spectroscopy;
EPR — electron paramagnetic resonance;
FEC — fluoroethylene carbonate;
ICE — initial Coulombic efficiency;
LIB — lithium-ion battery;
PAN — polyacrylonitrile;
PANI — polyaniline;
PC — propylene carbonate;
PDF — pair distribution function;
PET — polyethylene terephthalate;
PFA — perfluoroalkoxyalkane;
PIB — potassium-ion battery;
PP — polypyrrol;
PTFE — polytetrafluoroethylene;
RS — Raman spectroscopy;
SAXS — small-angle X-ray scattering;
SEI — solid electrolyte interphase;
SEM — scanning electron microscopy;
SIB — sodium-ion battery;
SSA_{BET} — BET specific surface area;
STM — scanning tunneling microscopy;
TEM — transmission electron microscopy;
XPS — X-ray photoelectron spectroscopy;
XRD — X-ray diffraction.

8. References

1. Z.Yang, J.Zhang, M.C.Kintner-Meyer, X.Lu, D.Choi, J.P.Lemmon, J.Liu. *Chem. Rev.*, **111**, 3577 (2011); https://doi.org/10.1021/cr100290v
2. A.A.Savina, A.O.Boev, E.D.Orlova, A.V.Morozov, A.M.Abakumov. *Russ. Chem. Rev.*, **92** (7), RCR5086 (2023); https://doi.org/10.59761/RCR5086
3. E.Irisarri, A.Ponrouch, M.R.Palacin. *J. Electrochem. Soc.*, **162**, A2476 (2015); https://doi.org/10.1149/2.0091514jes
4. E.C.Cengiz, J.Rizell, M.Sadd, A.Matic, N.Mozhzhukhina. *J. Electrochem. Soc.*, **168**, 120539 (2021); https://doi.org/10.1149/1945-7111/ac429b
5. W.Zhang, Y.Liu, Z.Guo. *Sci. Adv.*, **5.5**, eaav7412 (2019); https://doi.org/10.1126/sciadv.aav7412
6. H.Zhang, Y.Huang, H.Ming, G.Cao, W.Zhang, J.Ming, R.Chen. *J. Mater. Chem. A*, **8**, 1604 (2020); https://doi.org/10.1039/C9TA09984K
7. R.Li, J.Huang, J.Ren, L.Cao, J.Li, W.Li, G.Lu, A.Yu. *J. Alloys Compd.*, **818**, 152849 (2020); https://doi.org/10.1016/j.jallcom.2019.152849
8. T.Li, Z.Liu, Y.Gu, Y.Tang, F.Huang. *J. Alloys Compd.*, **817**, 152703 (2020); https://doi.org/10.1016/j.jallcom.2019.152703
9. W.Zhang, F.Zhang, F.Ming, H.N.Alshareef. *EnergyChem*, **1**, 100012 (2019); https://doi.org/10.1016/j.enchem.2019.100012
10. N.R.Khasanova, R.V.Panin, I.R.Cherkashchenko, M.V.Zakharkin, D.A.Novichkov, E.V.Antipov. *ACS Appl. Mater. Interfaces*, **15**, 30272 (2023); https://doi.org/10.1021/acsami.3c04576

11. K.Kubota, M.Dahbi, T.Hosaka, S.Kumakura, S.Komaba. *Chem. Record*, **18**, 459 (2018); https://doi.org/10.1002/tcr.201700057
12. Z.L.Xu, G.Yoon, K.Y.Park, H.Park, O.Tamwattana, S.J.Kim, W.M.Seong, K.Kang. *Nat. Commun.*, **10**, 2598 (2019); https://doi.org/10.1038/s41467-019-10551-z
13. U.Mittal, L.Djuandhi, N.Sharma, H.L.Andersen. *J. Phys. Energy*, **4**, 042001 (2022); https://doi.org/10.1088/2515-7655/ac8dc1
14. W.Shao, H.Shi, X.Jian, Z.S.Wu, F.Hu. *Adv. Energy Sustainability Res.*, **3**, 2200009 (2022); https://doi.org/10.1002/aesr.202200009
15. X.Dou, I.Hasa, D.Saurel, C.Vaalma, L.Wu, D.Buchholz, D.Bresser, S.Komaba, S.Passerini. *Mater. Today*, **23**, 87 (2019); https://doi.org/10.1016/j.mattod.2018.12.040
16. S.S.Tzeng, Y.G.Chr. *Mater. Chem. Phys*., **73**, 162 (2002); https://doi.org/10.1016/S0254-0584(01)00358-3
17. F.G.Emmerich. *Carbon*, **33**, 1709 (1995); https://doi.org/10.1016/0008-6223(95)00127-8
18. V.Uskoković. *Carbon Trends*, **5**, 100116 (2021); https://doi.org/10.1016/j.cartre.2021.100116
19. T.Noda, M.Inagaki. *Bull. Chem. Soc. Jpn.*, **37**, 1534 (1964); https://doi.org/10.1246/bcsj.37.1534
20. T.Noda, M.Inagaki, S.Yamada. *J. Non. Cryst. Solids*, **1**, 285 (1969); https://doi.org/10.1016/0022-3093(69)90026-X
21. V.M.Mel'nichenko, A.M.Sladkov, Yu.N.Nikulin. *Russ. Chem. Rev.*, **51**, 421 (1982); https://doi.org/10.1070/RC1982v051n05ABEH002851
22. R.E.Franklin. *Proc. R. Soc. Lond. A*, **209**, 196 (1951); https://doi.org/10.1098/rspa.1951.0197
23. R.E.Franklin. *Acta Crystallogr.*, **3**, 107 (1950); https://doi.org/10.1107/S0365110X50000264
24. G.M.Jenkins, K.Kawamura, L.L.Ban. *Proc. R. Soc. Lond. A*, **327**, 501 (1972); https://doi.org/10.1098/rspa.1972.0060
25. P.J.F.Harris. *Intern. Mater. Rev.*, **42**, 206 (1997); https://doi.org/10.1179/imr.1997.42.5.206
26. P.J.F.Harris. *Philosoph. Magazine*, **84**, 3159 (2004); https://doi.org/10.1080/14786430410001720363
27. P.J.F.Harris. *Critical Rev. Solid State Mater. Sci.*, **30**, 235 (2005); https://doi.org/10.1080/10408430500406265
28. Y.Wang, Z.Fan, P.Qian, T.Ala-Nissila, M.A.Caro. *Chem. Mater.*, **34**, 617 (2002); https://doi.org/10.1021/acs.chemmater.1c03279
29. V.LDeringer, C.Merlet, Y.Hu, T.H.Lee, J.A.Kattirtzi, O.Pecher, G.Csányi, S.R.Elliott, C.P.Grey. *Chem. Commun.*, **54**, 5988 (2018); https://doi.org/10.1039/C8CC01388H
30. C.Bommier, D.Mitlin, X.Ji. *Prog. Mater. Sci.*, **97**, 170 (2018); https://doi.org/10.1016/j.pmatsci.2018.04.006
31. Y.Kim, J.K.Kim, C.Vaalma, G.H.Bae, G.T.Kim, S.Passerini, Y.Kim. *Carbon*, **129**, 564 (2018); https://doi.org/10.1016/j.carbon.2017.12.059
32. X.Dou, C.Geng, D.Buchholz, S.Passerini. *APL Mater.*, **6**, 047501 (2018); https://doi.org/10.1063/1.5013132
33. Z.Li, Y.Chen, Z.Jian, H.Jiang, J.J.Razink, W.F. Stickle, J.C.Neuefeind, X.Ji. *Chem. Mater.*, **30**, 4536 (2018); https://doi.org/10.1021/acs.chemmater.8b00645
34. L.Xiao, H.Lu, Y.Fang, M.L.Sushko, Y.Cao, X.Ai, H.Yang, J.Liu. *Adv. Energy Mater.*, **8**, 1703238 (2018); https://doi.org/10.1002/aenm.201703238
35. H.Yamamoto, S.Muratsubaki, K.Kubota, M.Fukunishi, H.Watanabe, J.Kim, S.Komaba. *J. Mater. Chem. A*, **6**, 16844 (2018); https://doi.org/10.1039/C8TA05203D
36. R.Väli, A.Jänes, T.Thomberg, E.Lust. *J. Electrochem. Soc.*, **163**, A1619 (2016); https://doi.org/10.1149/2.0771608jes
37. Y.Lu, C.Zhao, X.Qi, Y.Qi, H.Li, X.Huang, L.Chen, Y.Hu. *Adv. Energy Mater.*, **8**, 1800108 (2018); https://doi.org/10.1002/aenm.201800108
38. C.Fan, R.Zhang, X.Luo, Z.Hu, W.Zhou, W.Zhang, J.Liu, J.Liu. *Carbon*, **205**, 353 (2023); https://doi.org/10.1016/j.carbon.2023.01.048
39. H.Wang, Z.Shi, J.Jin, C.Chong, C.Wang. *J. Electroanalyt. Chem.*, **755**, 87 (2015); https://doi.org/10.1016/j.jelechem.2015.07.032
40. A.Piotrowska, K.Kierzek, P.Rutkowski, J.Machnikowski. *J. Anal. Appl. Pyrolysis*, **102**, 1 (2013); https://doi.org/10.1016/j.jaap.2013.04.011
41. K.Gotoh, T.Ueda, T.Eguchi, K.Kawabata, K.Yamamoto, Y.Murakami, S.Hayakawa, H.Ishida. *Bull. Chem. Soc. Jpn.*, **82**, 1232 (2009); https://doi.org/10.1246/bcsj.82.1232
42. A.Kamiyama, K.Kubota, T.Nakano, S.Fujimura, S.Shiraishi, H.Tsukada, S.Komaba. *ACS Appl. Energy Mater.*, **3**, 135 (2019); https://doi.org/10.1021/acsaem.9b01972
43. C.M.Ghimbeu, B.Zhang, A.M. de Yuso, B.Réty, J.M.Tarascon. *Carbon*, **153**, 634 (2019); https://doi.org/10.1016/j.carbon.2019.07.026
44. C.Marino, J.Cabanero, M.Povia, C.Villevieille. *J. Electrochem. Soc.*, **165**, A1400 (2018); https://doi.org/10.1149/2.0681807jes
45. X.Lin, Y.Liu, H.Tan, B.Zhang. *Carbon*, **157**, 316 (2020); https://doi.org/10.1016/j.carbon.2019.10.045
46. I.El Moctar, Q.Ni, Y.Bai, F.Wu, C.Wu. *Funct. Mater. Lett.*, **11**, 1830003 (2018); https://doi.org/10.1142/S1793604718300037
47. H.Guo, K.Sun, Y.Lu, H.Wang, X.Ma, Z.Li, Y.S.Hu, D.Chen. *Chin. Phys. B*, **28**, 068203 (2019); https://doi.org/10.1088/1674-1056/28/6/068203
48. Y.Teng, M.Mo, Y.Li. *J. Electrochem. Eng. Conv. Stor.*, **15**, 041010 (2018); https://doi.org/10.1115/1.4040922
49. Z.E.Yu, Y.Lyu, Y.Wang, S.Xu, H.Cheng, X.Mu, J.Chu, R.Chen, Y.Liu, B.Guo. *Chem. Commun.*, **56**, 778 (2020); https://doi.org/10.1039/C9CC08221B
50. A.A.Arie, B.Tekin, E.Demir, R.Demir-Cakan. *Mater. Technol.*, **34**, 515 (2019); https://doi.org/10.1080/10667857.2019.1586087
51. N.Zhang, Q.Liu, W.Chen, M.Wan, X.Li, L.Wang, L.Xue, W.Zhang. *J. Power Sources*, **378**, 331 (2018); https://doi.org/10.1016/j.jpowsour.2017.12.054
52. A.Beda, P.L.Taberna, P.Simon, C.M.Ghimbeu. *Carbon*, **139**, 248 (2018); https://doi.org/10.1016/j.carbon.2018.06.036
53. Y.Wang, Y.Li, S.S.Mao, D.Ye, W.Liu, R.Guo, Z.Feng, J.Kong, J.Xie. *Sustainable Energy Fuels*, **3**, 717 (2019); https://doi.org/10.1039/C8SE00590G
54. M.K.Rybarczyk, Y.Li, M.Qiao, Y.S.Hu, M.M.Titirici, M.Lieder. *J. Energy Chem.*, **29**, 17 (2019); https://doi.org/10.1016/j.jechem.2018.01.025
55. Y.Zhang, X.Li, P.Dong, G.Wu, J.Xiao, X.Zeng, Y.Zhang, X.Sun. *ACS Appl. Mater. Interfaces*, **10**, 42796 (2018); https://doi.org/10.1021/acsami.8b13160
56. S.Zhang, Y.Li, M.Li. *Jom*, **70**, 1387 (2018); https://doi.org/10.1007/s11837-018-2789-0
57. Y.E.Zhu, H.Gu, Y.N.Chen, D.Yang, J.Wei, Z.Zhou. *Ionics*, **24**, 1075 (2018); https://doi.org/10.1007/s11581-017-2260-1
58. P.Wang, L.Fan, L.Yan, Z.Shi. *J. Alloys Compd.*, **775**, 1028 (2019); https://doi.org/10.1016/j.jallcom.2018.10.180
59. F.Wu, M.Zhang, Y.Bai, X.Wang, R.Dong, C.Wu. *ACS Appl. Mater. Interfaces*, **11**, 12554 (2019); https://doi.org/10.1021/acsami.9b01419
60. D.Y.Kim, D.H.Kim, S.H.Kim, E.K.Lee, S.K.Park, J.W.Lee, Y.S.Yun, S.Y.Choi, J.Kang. *Nanomaterials*, **9**, 793 (2019); https://doi.org/10.3390/nano9050793
61. J.Xiang, W.Lv, C.MU, J.Zhao, B.Wang. *J. Alloys Compd.*, **701**, 870 (2017); https://doi.org/10.1016/j.jallcom.2017.01.206
62. H.Wang, W.Yu, J.Shi, N.Mao, S.Chen, W.Liu. *Electrochim. Acta*, **188**, 103 (2016); https://doi.org/10.1016/j.electacta.2015.12.002
63. M.Dahbi, M.Kiso, K.Kubota, T.Horiba, T.Chafik, K.Hida, T.Matsuyama, S.Komaba. *J. Mater. Chem. A*, **5**, 9917 (2017); https://doi.org/10.1039/C7TA01394A
64. Z.Zhu, F.Liang, Z.Zhou, X.Zeng, D.Wang, P.Dong, J.Zhao, S.Sun, Y.Zhang, X.Li. *J. Mater. Chem. A*, **6**, 1513 (2018); https://doi.org/10.1039/C7TA07951F

65. F.Wu, L.Liu, Y.Yuan, Y.Li, Y.Bai, T.Li, J.Lu, C.Wu. *ACS Appl. Mater. Interfaces*, **10**, 27030 (2018); https://doi.org/10.1021/acsami.8b08380
66. A.A.Arie, H.Kristianto, H.Muljana, L.Stievano. *Fullerenes, Nanotubes and Carbon Nanostructures*, **27**, 953 (2019); https://doi.org/10.1080/1536383X.2019.1671372
67. H.Zhang, W.Xiao, W.Zhou, S.Chen, Y.Zhang. *Nanomaterials*, **9**, 553 (2019); https://doi.org/10.3390/nano9040553
68. C.Yu, H.Hou, X.Liu, Y.Yao, Q.Liao, Z.Dai, D.Li. *Int. J. Hydrogen Energy*, **43**, 3253 (2018); https://doi.org/10.1016/j.ijhydene.2017.12.151
69. G.P.Lakienko, Z.V.Bobyleva, M.O.Apostolova, Y.V.Sultanova, A.K.Dyakonov, M.V.Zakharkin, N.A.Sobolev, A.M.Alekseeva, O.A.Drozhzhin, A.M.Abakumov, E.V.Antipov. *Batteries*, **8**, 131 (2022); https://doi.org/10.3390/batteries8100131
70. E.Irisarri, N.Amini, S.Tennison, C.M.Ghimbeu, J.Gorka, C.Vix-Guterl, A.Ponrouch, M.R.Palacín. *J. Electrochem. Soc.*, **165**, A4058 (2018); https://doi.org/10.1149/2.1171816jes
71. B.Zhang, C.M.Ghimbeu, C.Laberty, C.Vix-Guterl, J.M.Tarascon. *Adv. Energy Mater.*, **6**, 1 (2016); https://doi.org/10.1002/aenm.201501588
72. J.Górka, C.Vix-Guterl, C.M.Ghimbeu. *C-J. Carbon Res.*, **2**, 24 (2016); https://doi.org/10.3390/c2040024
73. E.N.Abramova, N.Marat, D.P.Rupasov, P.A.Morozova, M.A.Kirsanova, A.M.Abakumov. *Carbon Trends*, **5**, 100089 (2021); https://doi.org/10.1016/j.cartre.2021.100089
74. C.Bommier, W.Luo, W.Y.Gao, A.Greaney, S.Ma, X.Ji. *Carbon*, **76**, 165-74 (2014); https://doi.org/10.1016/j.carbon.2014.04.064
75. M.Sevilla, A.B.Fuertes. *Chem.–Eur. J.*, **15**, 4195 (2009); https://doi.org/10.1002/chem.200802097
76. Nagmani, S.Puravankara. *ACS Appl. Energy Mater.*, **3**, 10045 (2020); https://doi.org/10.1021/acsaem.0c01750
77. F.Xie, Z.Xu, A.C.S.Jensen, F.Ding, H.Au, J.Feng, H.Luo, M.Qiao, Z.Guo, Y.Lu., A.J.Drew, Y.S.Hu, M.M.Titirici. *J. Mater. Chem. A*, **7**, 27567 (2019); https://doi.org/10.1039/C9TA11369J
78. Z.Xu, J.Wang, Z.Guo, F.Xie, H.Liu, H.Yadegari, M.Tebyetekerwa, M.P.Ryan, Y.S.Hu, M.M.Titirici. *Adv. Energy Mater.*, **12**, 2200208 (2022); https://doi.org/10.1002/aenm.202200208
79. M.Sevilla, A.B.Fuertes. *Carbon*, **47**, 2281 (2009); https://doi.org/10.1016/j.carbon.2009.04.026
80. Y.Jin, S.Sun, M.Ou, Y.Liu, C.Fan, X.Sun, J.Peng, Y.Li, Y.Qiu, P.Wei. *ACS Appl. Energy Mater.*, **1**, 2295 (2018); https://doi.org/10.1021/acsaem.8b00354
81. Z.V.Bobyleva, O.A.Drozhzhin, A.M.Alekseeva, K.A.Dosaev, G.S.Peters, G.P.Lakienko, T.I.Perfilyeva, N.A.Sobolev, K.I.Maslakov, S.V.Savilov, A.M.Abakumov, E.V.Antipov. *ACS Appl. Energy Mater.*, **6**, 181 (2023); https://doi.org/10.1021/acsaem.2c02716
82. T.Zhang, J.Mao, X.Liu, M.Xuan, K.Bi, X.L.Zhang, J.Hu, J.Fan, S.Chen, G.Shao. *RSC Adv.*, **7**, 41504 (2017); https://doi.org/10.1039/C7RA07231G
83. A.Beda, J.M.Le Meins, P.L.Taberna, P.Simon, C.M.Ghimbeu. *Sustainable Mater. Technol.*, **26**, e00227 (2020); https://doi.org/10.1016/j.susmat.2020.e00227
84. J.Wang, J.Zhao, X.He, Y.Qiao, L.Li, S.L.Chou. *Sustainable Mater. Technol.*, **33**, e00446 (2022); https://doi.org/10.1016/j.susmat.2022.e00446
85. D.Saurel, B.Orayech, B.Xiao, D.Carriazo, X.Li, T.Rojo. *Adv. Energy Mater.*, **8**, 1703268 (2018); https://doi.org/10.1002/aenm.201703268
86. H.Au, H.Alptekin, A.C.S.Jensen, E.Olsson, C.A.O'Keefe, T.Smith, M.Crespo-Ribadeneyra, T.F.Headen, C.P.Grey, Q.Cai, A.J.Drew, M.M.Titirici. *Energy Environ. Sci.*, **13**, 3469 (2020); https://doi.org/10.1039/D0EE01363C
87. P.S.Fontecoba. Doctoral Dissertation, Departamento de Química Inorgánica, Universidad del País Vasco (2017)
88. B.Zhang, M.Deschamps, M.Ammar, E.Raymundo-Piñero, L.Hennet, D.Batuk, J.M.Tarascon. *Adv. Mater. Technol.*, **2**, 1600227 (2017); https://doi.org/10.1002/admt.201600227
89. T.Kyotani, Z.Ma, A.Tomita. *Carbon*, **41**, 1451 (2003); https://doi.org/10.1016/S0008-6223(03)00090-3
90. Q.Li, X.Liu, Y.Tao, J.Huang, J.Zhang, C.Yang, Y.Zhang, S.Zhang, Y.Jia, Q.Lin. *Natl. Sci. Rev.*, **9**, nwac084 (2022); https://doi.org/10.1093/nsr/nwac084
91. J.Yang, X.Zhou, J.Li, Y.Zou, J.Tang. *Mater. Chem. Phys.*, **135**, 445 (2012); https://doi.org/10.1016/j.matchemphys.2012.05.006
92. A.Kamiyama, K.Kubota, D.Igarashi, Y.Youn, Y.Tateyama, H.Ando, K.Gotoh, S.Komaba. *Angew. Chem., Int. Ed.*, **60**, 5114 (2021); https://doi.org/10.1002/ange.202013951
93. X.Yin, Z.Lu, J.Wang, X.Feng, S.Roy, X.Liu, Y.Yang, Y.Zhao, J.Zhang. *Adv. Mater.*, **34**, 2109282 (2022); https://doi.org/10.1002/adma.202109282
94. Z.Lu, J.Wang, W.Feng, X.Yin, X.Feng, S.Zhao, C.Li, R.Wang, Q.Huang, Y.Zhao. *Adv. Mater.*, **35**, 2211461 (2023); https://doi.org/10.1002/adma.202211461
95. D.Igarashi, Y.Tanaka, K.Kubota, R.Tatara, H.Maejima, T.Hosaka, S.Komaba. *Adv. Energy Mater.*, **13**, 2302647 (2023); https://doi.org/10.1002/aenm.202302647
96. J.Wu, Z.Pan, Y.Zhang, B.Wang, H.Peng. *J. Mater. Chem. A*, **6**, 12932 (2018); https://doi.org/10.1039/C8TA03968B
97. H.Liu, M.Jia, B.Cao, R.Chen, X.Lv, R.Tang, F.Wu, B.Xu. *J. Power Sources*, **319**, 195 (2016); https://doi.org/10.1016/j.jpowsour.2016.04.040
98. L.Fu, K.Tang, K.Song, P.A.Van Aken, Y.Yu, J.Maier. *Nanoscale*, **6**, 1384 (2014); https://doi.org/10.1039/C3NR05374A
99. X.Shi, Y.Chen, Y.Lai, K.Zhang, J.Li, Z.Zhang. *Carbon*, **123**, 250 (2017); https://doi.org/10.1016/j.carbon.2017.07.056
100. Q.Jin, W.Li, K.Wang, P.Feng, H.Li, T.Gu, M.Zhou, W.Wang, S.Cheng, K.Jiang. *J. Mater. Chem. A*, **7**, 10239 (2019); https://doi.org/10.1039/C9TA02107H
101. S.Alvin, C.Chandra, J.Kim. *Chem. Eng. J.*, **391**, 123576 (2020); https://doi.org/10.1016/j.cej.2019.123576
102. Z.Li, C.Bommier, Z.S.Chong, Z.Jian, T.W.Surta, X.Wang, Z.Xing, J.C.Neuefeind, W.F.Stickle, M.Dolgos, P.A.Greaney, X.Ji. *Adv. Energy Mater.*, **7**, 1602894 (2017); https://doi.org/10.1002/aenm.201602894
103. Y.Wang, C.Wang, Y.Wang, H.Liu, Z.Huang. *ACS Appl. Mater. Interfaces*, **8**, 18860 (2016); https://doi.org/10.1021/acsami.6b04774
104. l.Xiao, Y.Cao, W.A.Henderson, M.L.Sushko, Y.Shao, J.Xiao, W.Wang, M.H.Engelhard, Z.Nie, J.Liu. *Nano Energy*, **19**, 279 (2016); https://doi.org/10.1016/j.nanoen.2015.10.034
105. H.Wang, Z.Wu, F.Meng, D.Ma, X.Huang, L.Wang, X.Zhang. *ChemSusChem*, **6**, 56 (2013); https://doi.org/10.1002/cssc.201200680
106. Z.Wang, L.Qie, L.Yuan, W.Zhang, X.Hu, Y.Huang. *Carbon*, **55**, 328 (2013); https://doi.org/10.1016/j.carbon.2012.12.072
107. U.N.Maiti, W.J.Lee, J.M.Lee, Y.Oh, J.Y.Kim, J.E.Kim, J.Shim, T.H.Han, S.O.Kim. *Adv. Mater.*, **26**, 40 (2014); https://doi.org/10.1002/adma.201303265
108. M.Chen, W.Wang, X.Liang, S.Gong, J.Liu, Q.Wang, S.Guo, H.Yang. *Adv. Energy Mater.*, **8**, 1800171 (2018); https://doi.org/10.1002/aenm.201800171
109. M.Wang, Y.Yang, Z.Yang, L.Gu, Q.Chen, Y.Yu. *Adv. Sci.*, **4**, 1600468 (2017); https://doi.org/10.1002/advs.201600468
110. F.Zhang, D.Qin, J.Xu, Z.Liu, Y.Zhao, X.Zhang. *Electrochim. Acta*, **303**, 140 (2019); https://doi.org/10.1016/j.electacta.2019.02.067
111. Y.Liu, H.Dai, L.Wu, W.Zhou, L.He, W.Wang, W.Yan, Q.Huang, L.Fu, Y.Wu. *Adv. Energy Mater.*, **9**, 1901379 (2019); https://doi.org/10.1002/aenm.201901379
112. D.Saurel, J.Segalini, M.Jauregui, A.Pendashteh, B.Daffos, P.Simon, M.Casas-Cabanas. *Energy Storage Mater.*, **21**, 162 (2019); https://doi.org/10.1016/j.ensm.2019.05.007

113. M.M.Titirici, M.Antonietti, N.Baccile. *Green Chem.*, **10**, 1204 (2008); https://doi.org/10.1039/b807009a
114. A.Gomez-Martin, J.Martinez-Fernandez, M.Ruttert, M.Winter, T.Placke, J.Ramirez-Rico. *Chem. Mater.*, **31**, 7288 (2019); https://doi.org/10.1021/acs.chemmater.9b01768
115. N.J.Song, N.Guo, C.Ma, Y.Zhao, W.Li, B.Li. *Molecules*, **28**, 3595 (2023); https://doi.org/10.3390/molecules28083595
116. Y.Shen, S.Sun, M.Yang, X.Zhao. *J. Alloys Compd.*, **784**, 1290 (2019); https://doi.org/10.1016/j.jallcom.2019.01.021
117. P.R.Lu, J.L.Xia, X.L.Dong. *ACS Sustainable Chem. Eng.*, **7**, 14841 (2019); https://doi.org/10.1021/acssuschemeng.9b02906
118. L.Li, C.Fan, Y.Tang, B.Zeng. *Int. J. Energy Res.*, **43**, 4987 (2019); https://doi.org/10.1002/er.4593
119. C.Chen, M.Wu, Y.Wang, K.Zaghib. *J. Power Sources*, **444**, 227310 (2019); https://doi.org/10.1016/j.jpowsour.2019.227310
120. Q.Wang, C.Gao, W.Zhang, S.Luo, M.Zhou, Y.Liu, R.Liu, Y.Zhang, Z.Wang, A.Hao. *Electrochim. Acta*, **324**, 134902 (2019); https://doi.org/10.1016/j.electacta.2019.134902
121. G.Murali, S.Harish, S.Ponnusamy, J.Ragupathi, H.A.Therese, M.Navaneethan, C.Muthamizhchelvan. *Appl. Surf. Sci.*, **492**, 464 (2019); https://doi.org/10.1016/j.apsusc.2019.06.142
122. K.Wang, Y.Xu, Y.Li, V.Dravid, J.Wu, Y.Huang. *J. Mater. Chem. A*, **7**, 3327 (2019); https://doi.org/10.1039/C8TA11510A
123. B.Ma, Y.Huang, Z.Nie, X.Qiu, D.Su, G.Wang, J.Yuan, X.Xie, Z.Wu. *RSC Adv.*, **9**, 20424 (2019); https://doi.org/10.1039/C9RA03345A
124. Z.Yuan, L.Si, X.Zhu. *J. Mater. Chem. A*, **3**, 23403 (2015); https://doi.org/10.1039/C5TA07223A
125. Y.Li, Y.Hu, M.M.Titirici, L.Chen, X.Huang. *Adv. Energy Mater.*, **6**, 1600659 (2016); https://doi.org/10.1002/aenm.201600659
126. D.Damodar, S.Ghosh, M.U.Rani, S.K.Martha, A.S.Deshpande. *J. Power Sources*, **438**, 227008 (2019); https://doi.org/10.1016/j.jpowsour.2019.227008
127. Y.Li, Y.Lu, Q.Meng, A.C.S.Jensen, Q.Zhang, Q.Zhang, Y.Tong, Y.Qi, L.Gu, M.M.Titirici. *Adv. Energy Mater.*, **9**, 1902852 (2019); https://doi.org/10.1002/aenm.201902852
128. M.E.Lee, H.W.Kwak, H.J.Jin, Y.S.Yun. *ACS Sustainable Chem. Eng.*, **7**, 12734 (2019); https://doi.org/10.1021/acssuschemeng.9b00971
129. Z.Zhou, Z.Gu, Y.He, D.Peng, C.Bao, H.Liu. *Int. J. Electrochem. Sci.*, **14**, 6976 (2019); https://doi.org/10.20964/2019.07.79
130. K.Kubota, S.Shimadzu, N.Yabuuchi, S.Tominaka, S.Shiraishi, M.Abreu-Sepulveda, A.Manivannan, K.Gotoh, M.Fukunishi, M.Dahbi, S.Komaba. *Chem. Mater.*, **32**, 2961 (2020); https://doi.org/10.1021/acs.chemmater.9b05235
131. Z.V.Bobyleva, M.O.Apostolova, G.P.Lakienko, A.M.Alekseeva, O.A.Drozhzhin, E.V.Antipov. *Chem. Technol. Fuels Oils*, **57**, 871 (2022); https://doi.org/10.1007/s10553-022-01320-8
132. V.Simone, A.Boulineau, A.de Geyer, D.Rouchon, L.Simonin, S.Martinet. *J. Energy Chem.*, **25**, 761 (2016); https://doi.org/10.1016/j.jechem.2016.04.016
133. K.Wang, Y.Jin, S.Sun, Y.Huang, J.Peng, J.Luo, Q.Zhang, Y.Qiu, C.Fang, J.Han. *ACS Omega*, **2**, 1687 (2017); https://doi.org/10.1021/acsomega.7b00259
134. G.Hasegawa, K.Kanamori, N.Kannari, J.Ozaki, K.Nakanishi, T.Abe. *J. Power Sources*, **318**, 41 (2016); https://doi.org/10.1016/j.jpowsour.2016.04.013
135. S.Alvin, D.Yoon, C.Chandra, H.S.Cahyadi, J.H.Park, W.Chang, K.Y.Chung, J.Kim. *Carbon*, **145**, 67 (2019); https://doi.org/10.1016/j.carbon.2018.12.112
136. C.Vaalma, G.A.Giffin, D.Buchholz, S.Passerini. *J. Electrochem. Soc.*, **163**, A1295 (2016); https://doi.org/10.1149/2.0921607jes
137. W.Li, J.Huang, L.Feng, L.Cao, Y.Ren, R.Li, Z.Xu, J.Li, C.Yao. *J. Alloys Compd.*, **716**, 210 (2017); https://doi.org/10.1016/j.jallcom.2017.05.062
138. C.Bommier, T.W.Surta, M.Dolgos, X.Ji. *Nano Lett.*, **15**, 5888 (2015); https://doi.org/10.1021/acs.nanolett.5b01969
139. J.K.Mathiesen, R.Väli, M.Härmas, E.Lust, J.F.Von Bülow, K.M.Jensen, P.Norby. *J. Mater. Chem. A*, **7**, 11709 (2019); https://doi.org/10.1039/C9TA02413A
140. J.M.Stratford, P.K.Allan, O.Pecher, P.A.Chater, C.P.Grey. *Chem. Comm.*, **52**, 12430 (2016); https://doi.org/10.1039/C6CC06990H
141. J.M.Stratford, A.K.Kleppe, D.S.Keeble, P.A.Chater, S.S.Meysami, C.J.Wright, J.Barker, M.M.Titirici, P.K.Allan, C.P.Grey. *J. Am. Chem. Soc.*, **143**, 14274 (2021); https://doi.org/10.1021/jacs.1c06058
142. A.M.Balagurov, I.A.E.Bobrikov, N.Y.Samoylova, O.A.Drozhzhin, E.V.Antipov. *Russ. Chem. Rev.*, **83**, 1120 (2014); https://doi.org/10.1070/RC2014v083n12ABEH004473
143. X.He, J.Liao, Z.Tang, L.Xiao, X.Ding, Q.Hu, Z.Wen, C.Chen. *J. Power Sources*, **396**, 533 (2018); https://doi.org/10.1016/j.jpowsour.2018.06.073
144. K.Jurkiewicz, M.Pawlyta, D.Zygadło, D.Chrobak, S.Duber, R.Wrzalik, A.Ratuszna, A.Burian. *J. Mater. Sci.*, **53**, 3509 (2018); https://doi.org/10.1007/s10853-017-1753-7
145. A.Sadezky, H.Muckenhuber, H.Grothe, R.Niessner, U.Pöschl. *Carbon*, **43**, 1731 (2005); https://doi.org/10.1016/j.carbon.2005.02.018
146. M.A.Pimenta, G.Dresselhaus, M.S.Dresselhaus, L.G.Cancado, A.Jorio, R.Saito. *Phys. Chem. Chem. Phys.*, **9**, 1276 (2007); https://doi.org/10.1039/B613962K
147. C.Thomsen, S.Reich. *Phys. Rev. Lett.*, **85**, 5214 (2000); https://doi.org/10.1103/PhysRevLett.85.5214
148. A.A.Ishenko, G.V.Fetisov, L.A.Aslanov. In *Nanokremnii: Svoistva, Poluchenie, Primenenie, Metody Issledovaniya i Kontrolya*. *(Nanosilicon: Properties, Production, Application, Methods of Research and Control)*. (Moscow: Fizmatlit, 2011). 405 p.
149. R.Morita, K.Gotoh, K.Kubota, S.Komaba, K.Hashi, T.Shimizu, H.Ishida. *Carbon*, **145**, 712 (2019); https://doi.org/10.1016/j.carbon.2019.01.080
150. M.P.Mercer, M.Nagarathinam, E.M.Gavilán-Arriazu, A.Binjrajka, S.Panda, H.Au, M.Crespo-Ribadeneyra, M.M.Titirici, E.P.M.Leiva, H.E.Hoster. *J. Mater. Chem. A*, **11**, 6543 (2023); https://doi.org/10.1039/D2TA09406A
151. A.Beda, C.Vaulot, C.M.Ghimbeu. *J. Mater. Chem. A*, **9**, 937 (2021); https://doi.org/10.1039/D0TA10088A
152. A.Beda, C.Vaulot, F.Rabuel, M.Morcrette, C.M.Ghimbeu. *Energy Adv.*, **1**, 185 (2022); https://doi.org/10.1039/D2YA00004K
153. A.Beda, F.Rabuel, M.Morcrette, S.Knopf, P.L.Taberna, P.Simon, C.M.Ghimbeu. *J. Mater. Chem. A*, **9**, 1743 (2021); https://doi.org/10.1039/D0TA07687B
154. S.M.Jafari, M.Khosravi, M.Mollazadeh. *Electrochim. Acta*, **203**, 9 (2016); https://doi.org/10.1016/j.electacta.2016.03.028
155. K.Nakabayashi, H.Yi, D.Y.Ryu, D.Chung, J.Miyawaki, S.H.Yoon. *Chem. Lett.*, **48**, 753 (2019); https://doi.org/10.1246/cl.190230
156. A.S.Vyacheslavov, E.A.Pomerantseva. *Izmerenie Ploshchadi Poverkhnosti i Poristosti Metodom Kapillyarnoi Kondensatsii Azota. Metedologicheskaya Razrabotka*. *(Measurement of Surface Area and Porosity Using Capillary Nitrogen Condensation. Methodological Development)*. (Moscow: MSU, 2006). P. 18
157. F.A.L.Dullien. In *Porous Media: Fluid Transport and Pore Structure*. (New York: Academic Press, 2012). P. 180
158. A.P.Karnaukhov. In *Adsorbtsiya*. *Tekstura Dispersnykh i Poristykh Materialov*. *(Adsorption. Texture of Dispersed and Porous Materials)*. (Novosibirsk: Nauka, 1999). 470 p.
159. C.Buttersack. *Phys. Chem. Chem. Phys.*, **21**, 5614 (2019) https://doi.org/10.1039/C8CP07751G
160. Z.Zhang. Doctoral Dissertation. Universite Paris-Est (2014)
161. Z.Jian, Z.Xing, C.Bommier, Z.Li, X.Ji. *Adv. Energy Mater.*, **6**, 1501874 (2016); https://doi.org/10.1002/aenm.201501874

162. D.Datta, J.Li, V.B.Shenoy. *ACS Appl. Mater. Interfaces*, **6**, 1788 (2014); https://doi.org/10.1021/am404788e
163. V.V.Sachkov. *Omskiy Nauchnyy Vestnik*, **5**, 1140118 (2020); https://doi.org/10.25206/1813-8225-2020-173-114-118
164. L.A.Openov, A.I.Podlivaev. *Phys. Solid State*, **57**, 1477 (2015); https://doi.org/10.1134/S1063783415070240
165. F.Béguin, F.Chevallier, C.Vix-Guterl, S.Saadallah, V.Bertagna, J.N.Rouzaud, E.Frackowiak. *Carbon*, **43**, 2160 (2005) https://doi.org/10.1016/j.carbon.2005.03.041
166. J.Yang, Z.Ju, Y.Jiang, Z.Xing, B.Xi, J.Feng, S.Xiong. *Adv. Mater.*, **30**, 1700104 (2018); https://doi.org/10.1002/adma.201700104
167. C.Bommier, X.Ji, P.A.Greaney. *Chem. Mater.*, **31**, 658 (2018); https://doi.org/10.1021/acs.chemmater.8b01390
168. A.Ponrouch, A.R.Goñi, M.R.Palacin. *Electrochem. Commun.*, **27**, 85 (2013); https://doi.org/10.1016/j.elecom.2012.10.038
169. C.Bommier, D.Leonard, Z.Jian, W.F.Stickle, P.A.Greaney, X.Ji. *Adv. Mater. Interfaces*, **3**, 1600449 (2016); https://doi.org/10.1002/admi.201600449
170. J.Deng, M.Li, Y.Wang. *Green Chem.*, **18**, 4824 (2016); https://doi.org/10.1039/C6GC01172A
171. G.Hasegawa, K.Kanamori, N.Kannari, J.Ozaki, K.Nakanishi, T.Abe. *ChemElectroChem*, **2**, 1917 (2015); https://doi.org/10.1002/celc.201500412
172. X.Zhao, Y.Ding, Q.Xu, X.Yu, Y.Liu, H.Shen. *Adv. Energy Mater.*, **9**, 1803648 (2019); https://doi.org/10.1002/aenm.201803648
173. X.Yu, L.Xin, X.Li, Z.Wu, Y.Liu. *Mater. Today*, **59**, 25 (2022); https://doi.org/10.1016/j.mattod.2022.07.013
174. R.Dugas, B.Zhang, P.Rozier, J.M.Tarascon. *J. Electrochem. Soc.*, **163**, A867 (2016); https://doi.org/10.1149/2.0051605jes
175. B.Zhang, R.Dugas, G.Rousse, P.Rozier, A.M.Abakumov, J.M.Tarascon. *Nat. Commun.*, **7**, 1 (2016); https://doi.org/10.1038/ncomms10308
176. J.M.De Ilarduya, L.Otaegui, M.Galcerán, L.Acebo, D.Shanmukaraj, T.Rojo, M.Armand. *Electrochim. Acta*, **321**, 134693 (2019); https://doi.org/10.1016/j.electacta.2019.134693
177. I.Moeez, H.G.Jung, H.D.Lim, K.Y.Chung. *ACS Appl. Mater. Interfaces*, **11**, 41394 (2019); https://doi.org/10.1021/acsami.9b14381
178. M.Liu, J.Zhang, S.Guo, B.Wang, Y.Shen, X.Ai, H.Yang, J.Qian. *ACS Appl. Mater. Interfaces*, **12**, 17620 (2020); https://doi.org/10.1021/acsami.0c02230
179. R.P.Kapaev, K.J.Stevenson. *J. Mater. Chem. A*, **9**, 11771 (2021); https://doi.org/10.1039/D1TA01460A
180. B.Shen, Y.You, Y.Niu, Y.Li, C.Dai, L.Hu, B.Guo, J.Jiang, S.Bao, M.Xu. *ACS Appl. Mater. Interfaces*, **10**, 16581 (2018); https://doi.org/10.1021/acsami.8b03986
181. Патент РФ 2731884C1 (2020)
182. W.Luo, C.Bommier, Z.Jian, X.Li, R.Carter, S.Vail, Y.Lu, J.J.Lee, X.Ji. *ACS Appl. Mater. Interfaces*, **7**, 2626 (2015); https://doi.org/10.1021/am507679x
183. A.Beda, C.Villevieille, P.L.Taberna, P.Simon, C.M.Ghimbeu. *J. Mater. Chem. A*, **8**, 5558 (2020); https://doi.org/10.1039/C9TA13189B
184. A.Ponrouch, M.R.Palacín. *Electrochem. Commun.*, **54**, 51 (2015); https://doi.org/10.1016/j.elecom.2015.03.002
185. F.Xie, Z.Xu, A.C.S.Jensen, H.Au, Y.Lu, V.Araullo-Peters, A.J.Drew, Y.S.Hu, M.M.Titirici. *Adv. Funct. Mater.*, **29**, 1901072 (2019); https://doi.org/10.1002/adfm.201901072
186. C.Bommier, X.Ji. *Small*, **14**, 1 (2018); https://doi.org/10.1002/smll.201703576
187. H.D.Asfaw, R.Gond, A.Kotronia, C.W.Tai, R.Younesi. *Sustainable Mater. Technol.*, **32**, e00407 (2022); https://doi.org/10.1016/j.susmat.2022.e00407
188. G.G.Eshetu, G.A.Elia, M.Armand, M.Forsyth, S.Komaba, T.Rojo, S.Passerini. *Adv. Energy Mater.*, **10**, 2000093 (2020); https://doi.org/10.1002/aenm.202000093
189. E.V.Beletskii, E.V.Alekseeva, O.V.Levin. *Russ. Chem. Rev.*, **91** (3), RCR5030 (2022); https://doi.org/10.1070/RCR5030
190. H.S.Hirsh, B.Sayahpour, A.Shen, W.Li, B.Lu, E.Zhao, M.Zhang, Y.S.Meng. *Energy Storage Mater.*, **42**, 78 (2021); https://doi.org/10.1016/j.ensm.2021.07.021
191. X.Yi, X.Li, J.Zhong, S.Wang, Z.Wang, H.Guo, J.Wang, G.Yan. *Adv. Funct. Mater.*, **32**, 2209523 (2022); https://doi.org/10.1002/adfm.202209523
192. J.Pan, Y.Sun, Y.Yan, L.Feng, Y.Zhang, A.Lin, F.Huang, J.Yang. *JACS Au*, **1**, 1208 (2021); https://doi.org/10.1021/jacsau.1c00158
193. D.H.Kim, B.Kang, H.Lee. *J. Power Sources*, **423**, 137 (2019); https://doi.org/10.1016/j.jpowsour.2019.03.047
194. T.Hosaka, K.Kubota, A.S.Hameed, S.Komaba. *Chem. Rev.*, **120**, 6358 (2020); https://doi.org/10.1002/9783527610426.bard110019
195. K.Takada, Y.Yamada, E.Watanabe, J.Wang, K.Sodeyama, Y.Tateyama, K.Hirata, T.Kawase, A.Yamada. *ACS Appl. Mater. Interfaces*, **9**, 33802 (2017); https://doi.org/10.1021/acsami.7b08414
196. J.Patra, H.T.Huang, W.Xue, C.Wang, A.S.Helal, J.Li, J.K.Chang. *Energy Storage Mater.*, **16**, 146 (2019); https://doi.org/10.1016/j.ensm.2018.04.022
197. D.M.C.Ould, S.Menkin, C.A.O'Keefe, F.Coowar, J.Barker, C.P.Grey, D.S.Wright. *Meet. Abstr.*, **MA2022-01**, 498 (2022); https://doi.org/10.1149/MA2022-013498mtgabs
198. Y.Morikawa, Y.Yamada, K.Doi, S.I.Nishimura, A.Yamada. *Electrochemistry*, **88**, 151 (2020); https://doi.org/10.5796/electrochemistry.19-00073
199. L.O.S.Colbin, R.Mogensen, A.Buckel, Y.Wang, A.J.Naylor, J.Kullgren, R.Younesi. *Adv. Mater. Interfaces*, **8**, 2101135 (2021); https://doi.org/10.1002/admi.202101135
200. J.Welch, R.Mogensen, W.van Ekeren, H.Eriksson, A.J.Naylor, R.Younesi. *J. Electrochem. Soc.*, **169**, 120523 (2022); https://doi.org/10.1149/1945-7111/acaa5e
201. K.Niitani, S.Ushiroda, H.Kuwata, H.N.Ohata, Y.Shimo, M.Hozumi, T.Matsunaga, S.Nakanishi. *ACS Energy Lett.*, **7**, 145 (2021); https://doi.org/10.1021/acsenergylett.1c02307
202. G.Yan, D.Alves-Dalla-Corte, W.Yin, N.Madern, G.Gachot, J.M.Tarascon. *J. Electrochem. Soc.*, **165**, A1222-30 (2018); https://doi.org/10.1149/2.0311807jes
203. G.Yan, K.Reeves, D.Foix, Z.Li, C.Cometto, S.Mariyappan, M.Salanne, J.M.Tarascon. *Adv. Energy Mater.*, **9**, 1901431 (2019); https://doi.org/10.1002/aenm.201901431
204. N.S.Katorova, S.Y.Luchkin, D.P.Rupasov, A.M.Abakumov, K.J.Stevenson. *J. Chem. Phys.*, **152**, 194704 (2020); https://doi.org/10.1063/5.0003257
205. N.S.Katorova, S.S.Fedotov, D.P.Rupasov, N.D.Luchinin, B.Delattre, Y.M.Chiang, A.M.Abakumov, K.J.Stevenson. *ACS Appl. Energy Mater.*, **2**, 6051 (2019); https://doi.org/10.1021/acsaem.9b01173
206. H.Dai, Z.Zeng, X.Yang, M.Jiang, Y.Wang, Q.Huang, L.Liu, L.Fu, P.Zhang, Y.Wu. *Carbon*, **179**, 60 (2021); https://doi.org/10.1016/j.carbon.2021.03.058
207. Z.Wu, J.Zou, S.Shabanian, K.Golovin, J.Liu. *Chem. Eng. J.*, **427**, 130972 (2022); https://doi.org/10.1016/j.cej.2021.130972
208. B.Hou, Y.Wang, Q.Ning, W.Li, X.Xi, X.Yang, H.Liang, X.Feng, X.Wu. *Adv. Mater.*, **31**, 1903125 (2019); https://doi.org/10.1002/adma.201903125
209. H.Yang, R.Xu, Y.Yu. *Energy Storage Mater.*, **22**, 105 (2019); https://doi.org/10.1016/j.ensm.2019.01.003
210. X.Li, Y.Zhou, B.Deng, J.Li, Z.Xiao. *Front. Chem.*, **11**, 1162909 (2023); https://doi.org/10.3389/fchem.2023.1162909
211. J.Hu, Y.Xie, M.Yin, Z.Zhang. *J. Energy Chem.*, **49**, 327 (2020); https://doi.org/10.1016/j.jechem.2020.03.005
212. H.Gong, Y.Chen, S.Chen, C.Xu, Y.Yang, Y.Ye, Z.Huang, R.Ning, Y.Cui, Z.Bao. *ACS Energy Lett.*, **7**, 4417 (2022); https://doi.org/10.1021/acsenergylett.2c02130

213. K.Su, T.Jin, C.H.Zhang, R.Wang, S.Yuan, N.W.Li, L.Yu. *Chem. Eng. J.*, **450**, 138049 (2022); https://doi.org/10.1016/j.cej.2022.138049
214. K.Wang, Y.Xu, H.Wu, R.Yuan, M.Zong, Y.Li, V.Dravid, W.Ai, J.Wu. *Carbon*, **178**, 443 (2021); https://doi.org/10.1016/j.carbon.2020.11.095
215. L.Xie, C.Tang, Z.Bi, M.Song, Y.Fan, C.Yan, X.Li, F.Su, Q.Zhang, C.Chen. *Adv. Energy Mater.*, **11**, 2101650 (2021); https://doi.org/10.1002/aenm.202101650
216. Z.V.Bobyleva, O.A.Drozhzhin, K.A.Dosaev, A.Kamiyama, S.V.Ryazantsev, S.Komaba, E.V.Antipov. *Electrochim. Acta*, **354**, 136647 (2020); https://doi.org/10.1016/j.electacta.2020.136647
217. D.A.Stevens, J.R.Dahn. *J. Electrochem. Soc.*, **148**, A803 (2001); https://doi.org/10.1149/1.1379565
218. S.Ahn, M.Lagnoni, Y.Yuan, A.Ogarev, E.Vavrinyuk, G.Voynov, E.Barrett, A.Pelli, A.Atrashchenko, A.Platonov, S.Gurevich, M.Gorokhov, D.Rupasov, A.W.Robertson, R.A.House, L.R.Johnson, A.Bertei, D.V.Chernyshov. *ACS Appl. Energy Mater.*, **6**, 8455 (2023); https://doi.org/10.1021/acsaem.3c01280
219. H.Hijazi, Z.Ye, L.Zhang, J.Deshmukh, M.B.Johnson, J.R.Dahn, M.Metzger. *J. Electrochem. Soc.*, **170**, 070512 (2023); https://doi.org/10.1149/1945-7111/ace4fa
220. D.A.Stevens, J.R.Dahn. *J. Electrochem. Soc.*, **147**, 1271 (2000); https://doi.org/10.1149/1.1393348
221. S.Komaba, W.Murata, T.Ishikawa, N.Yabuuchi, T.Ozeki, T.Nakayama, A.Ogata, K.Gotoh, K.Fujiwara. *Adv. Funct. Mater.*, **21**, 3859 (2011); https://doi.org/10.1002/adfm.201100854
222. R.Alcántara, P.Lavela, G.F.Ortiz, J.L.Tirado. *Electrochem. Solid State Lett.*, **8**, A222 (2005); https://doi.org/10.1149/1.1870612
223. K.Gotoh, T.Ishikawa, S.Shimadzu, N.Yabuuchi, S.Komaba, K.Takeda, A.Goto, K.Deguchi, S.Ohki, K.Hashi, T.Shimizu, H.Ishida. *J. Power Sources*, **225**, 137 (2013); https://doi.org/10.1016/j.jpowsour.2012.10.025
224. Y.Cao, L.Xiao, M.L.Sushko, W.Wang, B.Schwenzer, J.Xiao, Z.Nie, L.V.Saraf, Z.Yang, J.Liu. *Nano Lett.*, **12**, 3783 (2012); https://doi.org/10.1021/nl3016957
225. J.Ding, H.Wang, Z.Li, A.Kohandehghan, K.Cui, Z.Xu, B.Zahiri, X.Tan, E.M.Lotfabad, B.C.Olsen, D.Mitlin. *ACS Nano*, **7**, 11004 (2013); https://doi.org/10.1021/nn404640c
226. S.Qiu, L.Xiao, M.L.Sushko, K.S.Han, Y.Shao, M.Yan, X.Liang, L.Mai, J.Feng, Y.Cao. *Adv. Energy Mater.*, **7**, 1700403 (2017); https://doi.org/10.1002/aenm.201700403
227. C.M.Ghimbeu, J.Górka, V.Simone, L.Simonin, S.Martinet, C.Vix-Guterl. *Nano Energy*, **44**, 327 (2018); https://doi.org/10.1016/j.nanoen.2017.12.013
228. F.Xie, Z.Xu, Z.Guo, M.M.Titirici. *Prog. Energy*, **2**, 042002 (2020); https://doi.org/10.1088/2516-1083/aba5f5
229. K.Gotoh, H.Ishida. *Carbon*, **78**, 633 (2014); https://doi.org/10.1016/j.carbon.2014.06.067
230. R.Morita, K.Gotoh, M.Fukunishi, K.Kubota, S.Komaba, N.Nishimura, T.Yumura, K.Deguchi, S.Ohki, T.Shimizu, H.Ishida. *J. Mater. Chem. A*, **4**, 13183 (2016); https://doi.org/10.1039/C6TA04273B
231. Y.Morikawa, S.Nishimura, R.Hashimoto, M.Ohnuma, A.Yamada. *Adv. Energy Mater.*, **10**, 1903176 (2019); https://doi.org/10.1002/aenm.201903176
232. J.S.Weaving, A.Lim, J.Millichamp, T.P.Neville, D.Ledwoch, E.Kendrick, P.F.Mcmillan, P.R.Shearing, C.A.Howard, D.J.L.Brett. *ACS Appl. Energy Mater.*, **3**, 7474 (2020); https://doi.org/10.1021/acsaem.0c00867
233. M.A. Reddy, M.Helen, A.Groß, M.Fichtner, H.Euchner. *ACS Energy Lett.*, **3**, 2851 (2018); https://doi.org/10.1021/acsenergylett.8b01761
234. H.Euchner, B.P.Vinayan, M.A.Reddy, M.Fichtner, A.Groß. *J. Mater. Chem. A*, **8**, 14205 (2020); https://doi.org/10.1039/D0TA04868B
235. N.Shimodaira, A.Masui. *J. Appl. Phys.*, **92**, 902 (2002); https://doi.org/10.1063/1.1487434
236. T.W.Surta, E.Koh, Z.Li, D.B.Fast, X.Ji, P.A.Greaney, M.R.Dolgos. *Adv. Energy Mater.*, **12**, 2200647 (2022); https://doi.org/10.1002/aenm.202200647
237. S.Alvin, H.S.Cahyadi, J.Hwang, W.Chang, S.K.Kwak, J.Kim. *Adv. Energy Mater.*, **10**, 1 (2020); https://doi.org/10.1002/aenm.202000283
238. L.Tao, L.Liu, R.Chang, H.He, P.Zhao, J.Liu. *J. Power Sources*, **463**, 228172 (2020); https://doi.org/10.1016/j.jpowsour.2020.228172
239. J.Xu, C.Fan, M.Ou, S.Sun, Y.Xu, Y.Liu, X.Wang, Q.Li, C.Fang, J.Han. *Chem. Mater.*, **34**, 4202 (2022); https://doi.org/10.1021/acs.chemmater.2c00646
240. W.Li, R.Zhang, Z.Chen, B.Fan, K.Xiao, H.Liu, P.Gao, J.Wu, C.Tu, J.Liu. *Small*, **17**, 2100397 (2021); https://doi.org/10.1002/smll.202100397
241. X.Lin, J.Huang, B.Zhang. *Carbon*, **143**, 138 (2019); https://doi.org/10.1016/j.carbon.2018.11.001
242. A.Tyagi, S.Puravankara. *Mater. Adv.*, **3**, 810 (2022); https://doi.org/10.1039/D1MA00731A
243. Y.Huang, Y.Wang, P.Bai, Y.Xu. *ACS Appl. Mater. Interfaces*, **13**, 38441 (2021); https://doi.org/10.1021/acsami.1c12150
244. T.G.Gul'misaryan, V.M.Kapustin, I.P.Levenberg. In *Tekhnicheskii Uglerod: Morfologiya*, *Svoistva*, *Proizvodstvo*. *(Carbon Black: Morphology, Properties, Production)*. (Moscow: Kauchuk i Pezina, 2017). 586 p.
245. K.Bowal, J.W.Martin, A.J.Misquitta, M.Kraft. *Combustion Sci. Technol.*, **191**, 747 (2019); https://doi.org/10.1080/00102202.2019.1565496
246. R.M.Mironenko, V.A.Likholobov, O.B.Belskaya. *Russ. Chem. Rev.*, **91** (1) RCR5017 (2022); https://doi.org/10.1070/RCR5017
247. Z.Xu, Z.Guo, R.Madhu, F.Xie, R.Chen, J.Wang, M.Tebyetekerwa, Y.S.Hu, M.M.Titirici. *Energy Environ. Sci.*, **14**, 6381 (2021); https://doi.org/10.1039/D1EE01346G